PAH and dust particles surface interaction. Catalytic hydrogenation of PAH molecules under vacuum conditions.

Gustavo A. Cruz-Diaz* +,§, Alessandra Ricca §,‡, Andrew L. Mattioda§

+Bay-Area Environmental Research Institute, Moffett Field, Mountain View, CA 94035.

§NASA Ames Research Center, Moffett Field, Mountain View, CA 94035.

‡Carl Sagan Center, SETI Institute, 189 Bernardo Avenue, Suite 200, Mountain View, CA 94043, USA

ABSTRACT. This work reports experiments on the catalytic interaction occurring between Polycyclic Aromatic Hydrocarbon (PAH) molecules TiO_2 and dust grain surfaces under vacuum conditions. The investigation sheds light on the potential catalytic pathways TiO_2 dust surfaces provide in the hydrogenation of PAH molecules, and the chemistry that can be driven by PAH-dust interactions under vacuum conditions. Naphthalene, anthracene, and coronene were chosen as the PAH molecules, while titanium dioxide was selected as the dust analog. PAH samples and dust analog mixtures were studied under vacuum for 24 hours while monitored via Diffuse

Reflectance Infrared Fourier Transform Spectroscopy (DRIFTS). The acquired spectra show that PAH molecules are hydrogenated when in contact with TiO_2 dust particles without the need for external energy or hydrogen sources. Our results suggest that linear PAHs undergo a similar hydrogenation process where the dominant species are fully hydrogenated PAHs. For condensed PAHs, the hydrogenation process yields partially hydrogenated molecules. Fully hydrogenated species can be identified by a band around 2960 cm^{-1}, while partially hydrogenated species produce a band around 2825 cm^{-1}. In the case of the production of hydrogenated species, our results suggest that smaller the PAH the faster the hydrogenation rate.

INTRODUCTION

Polycyclic Aromatic Hydrocarbons (PAHs) are detected through their near- and mid-infrared features in the Interstellar Medium (ISM)[1–7]. They are considered to be responsible for almost 20% of all the carbon in the universe. In protoplanetary disks, PAHs are assumed to contain about 10% of the total carbon[8]. PAHs are often detected around more evolved stars; for example, PAHs have been detected in almost 60% of disks surrounding intermediate-mass stars, like Herbig Ae/Be, while in only 8% of the disks surrounding T Tauri stars[8,9]. The infrared spectra of star and planet formation regions often show the presence of PAH emission features. This PAH emission originates from either the disk or the envelope, in regions with radii of 10 to 60 AU[4,10–13]. PAHs have also been detected in carbonaceous chondrites[14–17], asteroids[18,19], interplanetary dust particles, comets[20,21], and tentatively identified in the planetary satellites Iapetus and Phoebe[22]. The fact that they have been detected ubiquitously in space is why it is essential to study and understand the physics and chemistry involved in their life cycle.

The hydrogenation of PAH molecules has been the target of recent research to understand the formation and current abundance of H_2 in the interstellar medium. Mennella et al.[23] and Thrower et al.[24] investigated the hydrogenation of coronene thin films under ultra-high-vacuum conditions (but not the interaction between PAH and dust particles); they exposed the films to an atomic deuterium gas flow and recorded the thermal desorption of coronene and its dehydrogenated and hydrogenated counterparts. They concluded that neutral PAHs could play an essential catalytic role in the H_2 formation in dark clouds. Ferullo et al.[25] used a Density Functional Theory (DFT) approximation to study the formation of molecules using hydrogenated PAH molecules as catalysts. They not only observed the formation of H_2 but also the formation of H_2O molecules, arguing that the catalytic formation of water on hydrogenated PAH molecules could be a possible route for water formation in the cold interstellar medium. Cazaux et al.[26,27] exposed coronene molecules to a constant flux of H atoms to study the hydrogenation of coronene in gas-phase. Cazaux et al.[27] found that a favorable abundance for some configurations of hydrogenated coronene could exist in space. They also noted that the hydrogenation of coronene was not random; on the contrary, it follows a specific hydrogenation pattern.

PAHs have been used to explain the observed 3.3 μm band as aromatic compounds present C-H stretching bands around this frequency[1,28–31]. Likewise, bands observed between 3.4 to 3.6 μm have been attributed to the aliphatic C-H stretching modes. The addition of a hydrogen atom to PAH molecules breaks their aromaticity, creating two C-H bonds, which at the same time produce bands in the 3.4 to 3.6 μm region[32–41]. Nevertheless, it is still under debate if those

astronomical bands are the result of hydrogenated or substituted (a methyl group attached to the PAH molecule) compounds. Pauzat and Ellinger[39] modeled the gas-phase hydrogenation of different PAHs with different configurations. They compared their results with observations, concluding that only the hydrogenated family seems to contribute efficiently to the 3.4 to 3.6 μm bands, with this result nominating the hydrogenated PAHs as tentative carriers for the aliphatic bands observed in space. Mackie et al.[42] included anharmonicities in their theoretical calculations to better understand the aliphatic IR features of substituted PAHs and accurately predict the bands appearing between 3.1 to 3.6 μm. With their study, Mackie et al.[42] confirmed that the features at 3.40, 3.46, and 3.51 μm can be reproduced by a hydrogenated PAH. Then, they argued that the feature at 3.40 μm was attributed to in-plane CH-stretching modes, and the two features at 3.46, and 3.51 μm were attributed to out-of-plane CH-stretching modes in strong resonance with combination bands of paired CH-bending modes.

PAHs are often mentioned alongside dust particles, and sometimes they are even considered as dust itself[43–48]. Even though they seem to share an intricate relation, little is known about the interactions between PAH molecules and dust particles, even when they have been detected in carbonaceous chondrites, asteroids, interplanetary dust particles, and comets. Zhao et al.[49] studied the catalytic conversion of acetylene on SiC grain surfaces under vacuum conditions. They found that catalytic reactions using acetylene produced a surface PAH (ring-like structure) on SiC surfaces, mimicking the chemical processes in certain astrophysical environments. They concluded that PAH molecules could be formed through decomposition of a graphene-like

material, formed on the surface of SiC grains in carbon-rich circumstellar envelopes. These results highlight the importance of catalytic reactions on dust grains surfaces since they can play an essential role in space chemistry.

On Earth, PAHs can be native to the environment and also due to man-made pollution. They can be found in oil seeps, are produced by volcanic eruptions, forest fires, and by burning fossil fuels, coal, and are found in used lubricant oil[50]. PAHs do not degrade quickly; the larger their mass, the more difficult it is to degrade them. Due to their carcinogenic nature, it is essential to know how to transform them into less hazardous forms. In nature, PAHs can be degraded by volatilization, adsorption onto soil particles, photo-oxidation, and chemical oxidation, however microbial degradation is the primary (most prolific) process. Algae, bacteria, and fungi are microorganisms that breakdown the organic compounds by biotransformation and mineralization[50].

Alumina, active carbon, zeolites, and metal oxides are among the most commonly used catalyst in the industry, with Titanium dioxide (TiO_2) being the most common catalyst in the industry. It possesses high mechanical strength and thermal stability, as well as a highly-porous surface. TiO_2 has been continuously used in mineralizing toxic and nonbiodegradable hazardous materials due to its nontoxicity and high effectiveness[51–53]. TiO_2 exists in three physical states, namely anatase, rutile, and brookite. Anatase is the state most utilized for a broad range of catalytic processes. As a first step, this work focuses on the interaction of PAH molecules and a "simple" dust analog TiO_2 in its anatase form, given its catalytic properties. In future works,

PAH-mineral interactions will be studied utilizing more astrophysically relevant dust analogs, like olivines and pyroxenes, known to be present in meteorites alongside PAHs[54,55]. Hence, TiO_2 serves here as a tool to study the catalytic hydrogenation of PAHs. Nevertheless, TiO_2 has been suggested to be present in interstellar dust particles[56,57], and it has been proved that one grain of TiO_2 could be enough to kick-start the nucleation of silicate dust particles[58].

In this work, we analyze the interaction between the PAH molecules naphthalene, anthracene, and coronene, and TiO_2 surfaces under vacuum conditions. To further investigate our experimental data, existing and new theoretical calculations were used. The experimental data are compared with theoretical calculations. In the experimental protocol section, the sample preparation, the data collection, and the method used for calculations are described.

EXPERIMENTAL PROTOCOL

Sample preparation

Experiments were performed using a high-vacuum and low-temperature reaction chamber from Harrick Scientific Products. The set-up is composed of a modified high-vacuum chamber capable of achieving $1x10^{-7}$ torr. It is designed to perform DRIFTS (Diffus Reflectance Infrared Fourier Transform Spectroscopy) to monitor the evolution of dust particles *in situ*. A Praying Mantis DRIFTS accessory was used to focus and collect the IR beam probing the dust sample, see Figure 1.

Naphthalene ($C_{10}H_8$, 99% purity from Sigma Aldrich), anthracene ($C_{14}H_{10}$, 99% purity from Sigma Aldrich), and coronene ($C_{24}H_{12}$, 97% purity from Sigma Aldrich) were used in the experiments. Titanium(IV) dioxide (TiO_2 anatase, 99.6% from Alfa Aesar) was selected as the mineral/dust analog because of its catalytic properties. TiO_2 powder was ground using a mortar and pestle. This powder was then sieving using a 270 grid-size mesh limiting the size of dust particles in this study to about 53 μm and smaller. After sieving, the TiO_2 was weighed using a microbalance (JF Series, model JF2004, Analytical Balance). The weighed TiO_2 was then mixed with methanol (enough to soak the TiO_2 sample) in a glass beaker to remove any organic contaminant. The mixture of methanol and TiO_2 was put into an ultrasonic bath (FS20, Fisher Scientific) for 30 min. Methanol molecules attached to TiO_2 produce IR bands between 2840 - 2860 cm^{-1} and 2950 - 2965 cm^{-1} [59]. However, temperature-programmed desorption (TPD) experiments show that the bulk of methanol sublimates from the TiO_2 surface before reaching 400 K (126.85 ^{o}C)[60]. Thus, as a final step, the beaker containing the TiO_2 dust and the remaining methanol was heated to approximately 200 °C inside a furnace, to remove any remaining methanol and water molecules (from air exposure) on the dust particle surfaces. Naphthalene, anthracene, and coronene are solid compounds at room temperature. The previously treated TiO_2 powder was weighed for a second time selecting 0.1 grams. Similarly, an amount of 0.01 grams of PAH was weighed out. The TiO_2 powder and the PAH were mixed, maintaining a ratio of 10 to 1 by mass, respectively, and ground together using a mortar and pestle. The mixture was then deposited in the sample holder for analysis, see the image on the left in Figure 1.

Every PAH-TiO$_2$ experiment was conducted in triplicate to verify the reproducibility of the results. Following the steps described in the experimental protocol section, the PAH-mineral mixtures were placed under vacuum (1x10^{-7} torr) for 24 hours and regularly monitored (every 10 minutes for naphthalene and anthracene and every hour for coronene) via DRIFTS. The samples were kept at room temperature (i.e. no heating or cooling) and no UV irradiation was performed during this time. Thus any spectral changes observed are due to the interactions between the dust surfaces and the PAH molecules.

To avoid cross-contamination in the experiments, after the conclusion of each experiment, the vacuum chamber was cleaned in the following manner: the sample holder was emptied, and the entire chamber was rinsed with methanol. Next, the chamber was sealed, pumped out. The temperature inside the chamber was raised to 200 °C, removing any volatile molecules. The chamber was pumped until a vacuum of 1x10^{-7} torr was again achieved.

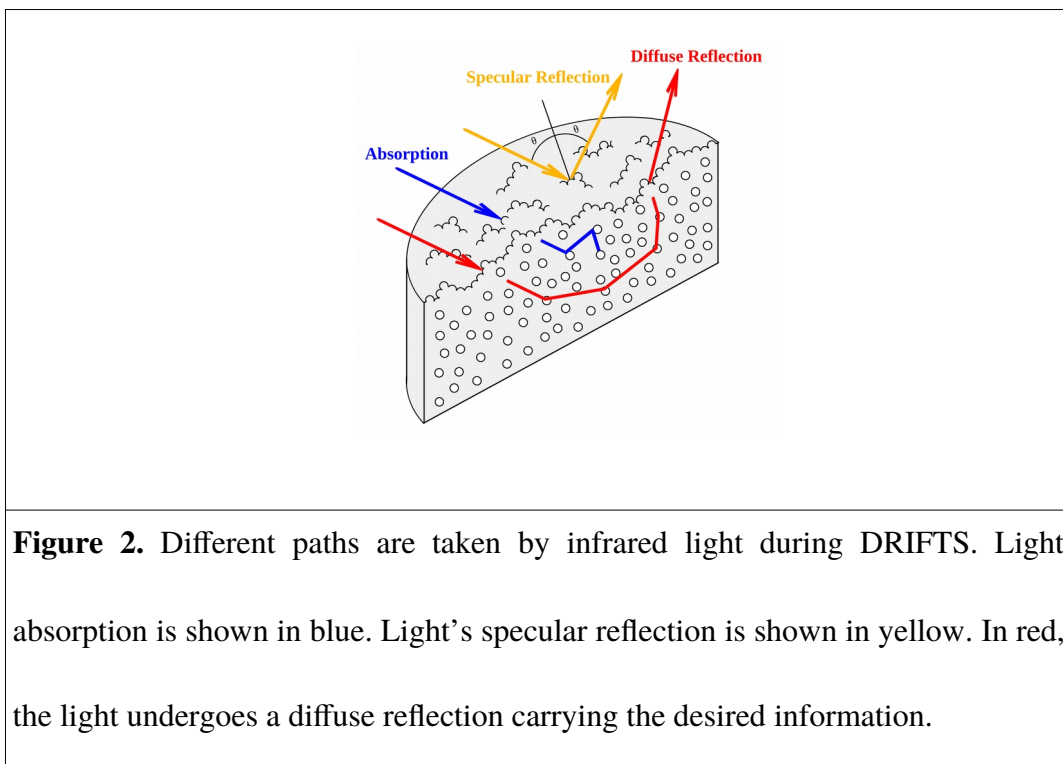**Figure 1.** Left: Harrick's low-temperature reaction chamber used for this study.
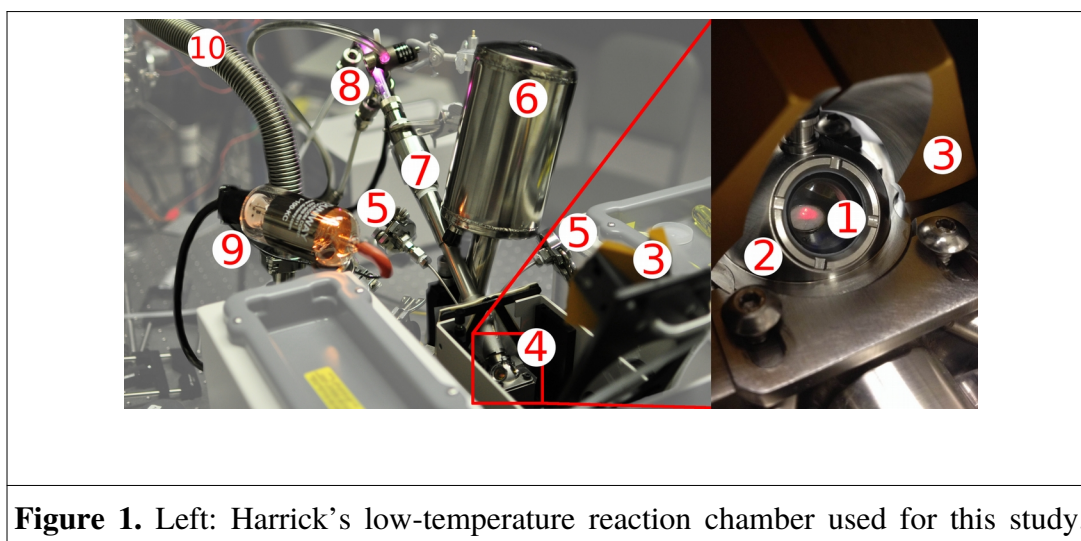
Right: close-up of the sample holder. The chamber is placed inside the Praying Mantis DRIFTS attachment, which, in turn, is located inside the FTIR spectrometer's sample compartment. Parabolic mirrors focus the infrared beam onto the sample surface and collect the scattered radiation for analysis. 1: Sample inside the vacuum chamber holder. 2: Dome used to seal the sample holder. 3: Praying Mantis' parabolic mirrors, which focus the IR beam on the sample. 4: Low temperature chamber inside the Praying Mantis DRIFTS unit. 5: Gas inlets/outlets. 6: Dewar for liquid N_2. 7: UV guidance tube. 8: Microwave-discharge hydrogen-flow lamp. 9: Ion gauge. 10: Vacuum bellow hose.

Data collection

The spectroscopic evolution of the sample was monitored *in situ* via DRIFTS. DRIFT spectroscopy is a technique developed for measurements of non-IR-transparent materials like dust grains[61]. Infrared spectra were recorded from 4000 to 450 cm^{-1} using a Biorad Excalibur FTS 4000 FTIR spectrometer, equipped with a potassium bromide (KBr) beamsplitter and an LN$_2$-cooled MCT detector. The Praying Mantis accessory is inserted into the sample compartment of the IR spectrometer. The light coming from the infrared source is focused onto the surface of the sample. This light can be absorbed, reflected (specular reflection), or diffuse reflected by the sample surface and bulk, see Figure 2. The likelihood of the process depends on the intrinsic characteristics of the material. The photons useful for DRIFTS are the ones that

diffuse through the sample containing information about the absorption properties of the material.

Figure 2. Different paths are taken by infrared light during DRIFTS. Light absorption is shown in blue. Light's specular reflection is shown in yellow. In red, the light undergoes a diffuse reflection carrying the desired information.

Theoretical Calculations

The molecular geometries have been fully optimized, and their harmonic frequencies computed using Density Functional Theory (DFT) and the Gaussian 16[62] suite of programs. All the structures are minima, i.e., they have no imaginary frequencies. The hybrid B3LYP[63,64] functional and the 4-31G basis set[65] have been used to be consistent with the spectra of hydrogenated PAHs already available in the NASA Ames PAH IR Spectroscopic Database (PAHdb, https://www.astrochemistry.org/pahdb/)[66,67]. The harmonic frequencies have been
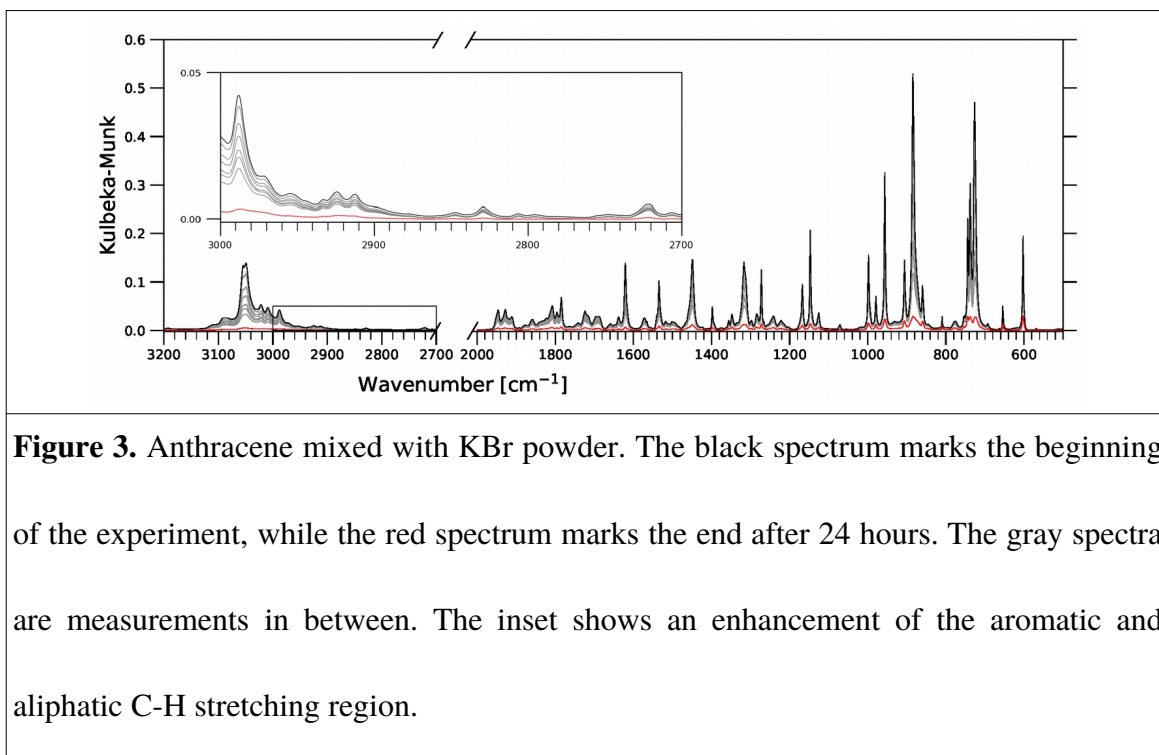
scaled using a single scaling factor of 0.958, which has been shown to bring the computed spectra in agreement with matrix-isolation spectra[68]. Synthetic spectra were obtained by broadening the integrated band intensities in wavenumber space by 5 cm^{-1}, consistent with the experimental bandwidths. The calculations do not include overtones, combination bands, or resonances (such as Fermi). The vibrational modes have been visualized using the Jmol (http://jmol.sourceforge.net) software to aid in the assignment of the infrared bands. The theoretical spectra of hydrogenated naphthalene and partially hydrogenated coronene were taken from the PAHdb database[66], whereas those for hydrogenated anthracene and fully hydrogenated coronene were computed as described above.

RESULTS

This study investigated catalytic interactions between PAH molecules and TiO$_2$ dust particle surfaces to understand the role particle surfaces play in the processing of PAH molecules, under vacuum conditions, with no external energy sources (i.e., UV photons).

Prior to the PAH-mineral experiments, naphthalene, anthracene, and coronene powders and the dust analog used in this investigation were mixed independently with potassium bromide (KBr) in a 1:10 mass ratio to obtain spectral baselines (see Figures 3 to 5). Given its low molecular weight, anthracene (as well as naphthalene) sublimates under vacuum hence, its spectral bands decrease as a function of time. In the case of coronene, a negligible sublimation occurs under vacuum conditions, as evidenced by the lack of a band decrease in the spectra of Figure 4. The

3000 to 2700 cm^{-1} aromatic and aliphatic C-H stretching region of both anthracene and coronene do not show the formation and growth of any new bands over time. In the case of titanium dioxide mixed with KBr, as shown in Figure 5, there is no loss of sample or growth of new features in the 3000 to 2700 cm^{-1} region over 24 hours. TiO$_2$ presents a strong and broad absorption band that extends from 1300 cm^{-1} to lower frequencies, peaking at 727 cm^{-1}, which obscures any other feature in this region. The observed changes for the PAH-mineral experiments are discussed in the following sections.
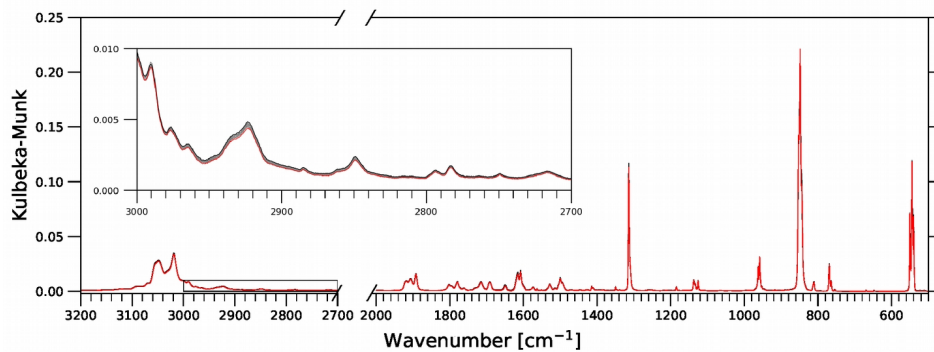

Figure 3. Anthracene mixed with KBr powder. The black spectrum marks the beginning of the experiment, while the red spectrum marks the end after 24 hours. The gray spectra are measurements in between. The inset shows an enhancement of the aromatic and aliphatic C-H stretching region.
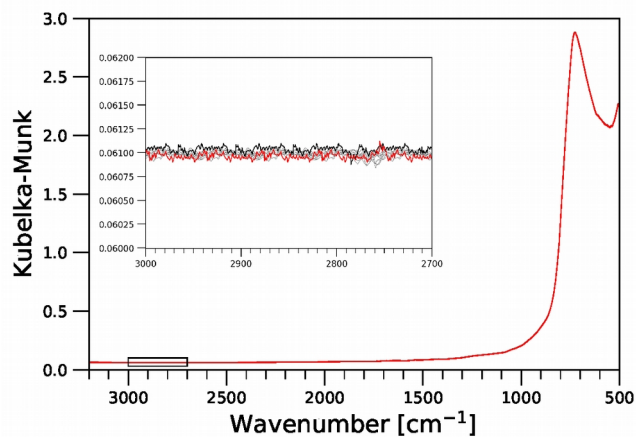
Figure 4. Coronene mixed with KBr powder. The black spectrum marks the beginning of the experiment, while the red spectrum marks the end after 24 hours. The gray spectra are measurements in between. The inset shows an enhancement of the aromatic and aliphatic C-H stretching region.

Figure 5. TiO₂ mixed with KBr powder. The black spectrum marks the beginning of the experiment, while the red spectrum marks the end after 24 hours. The gray spectra are

measurements in between. The inset shows an enhancement of the aliphatic C-H stretching region showing no evolution over time.

Naphthalene hydrogenation

In the top panel of Figure 6, the subtraction spectra of the naphthalene experiment are shown. Each subtraction spectrum was obtained by subtracting off the initial spectrum at time 0 minutes from the spectrum at T (T = 10 minutes to 24 hours). A subtraction factor of 1 (i.e., the full initial spectrum was subtracted off) resulted in part of the spectrum having "negative" absorbance bands. These negative bands are due to the loss of PAH molecules, as represented by the aromatic C-H stretching bands located above the 3000 cm^{-1} part of the spectrum. In this instance, the loss of PAH molecules is due to both the sublimation of naphthalene under vacuum conditions and the PAH's hydrogenation.

Although naphthalene sublimation occurs in these experiments, it does not impact the analysis or interpretation of the catalytic hydrogenation process. Even though, quantifying observed reactions using DRIFTS is difficult, as a reflectance standard is needed for quantification[61,69], an approximation for the rate of change (decrease) in the naphthalene spectra (by sublimation and hydrogenation) can be calculated. Integrating the naphthalene experimental aromatic bands in Figure 6 and using the A-values (band strength) listed in Sandford et al[70], the decreasing rate of naphthalene molecules is 9.3×10^{13} molecules cm^{-2} per minute.

New bands were observed growing at 2960, 2932, and 2861 cm^{-1} during the experiment, with shoulders detected at 2907, 2871, 2843, and 2825 cm^{-1} see Figure 6. Spectral features in this region of the spectrum are well known aliphatic C-H stretching bands. The presence of these bands indicates that hydrogenation of the naphthalene molecules occurs. In the bottom panel of Figure 6, the theoretical spectra for the various hydrogenated forms of naphthalene are shown. These theory data were taken from the NASA Ames PAHdb database to assign the experimentally observed bands. Table S1 shows the aliphatic bands' positions in the different hydrogenation products of naphthalene, drawn in Figure 6. These positions depend on the number of hydrogen atoms involved in the hydrogenation as well as where in the molecules they are positioned. The theoretical spectra shown in the bottom panel of Figure 6 and the values given in Table S1 were computed for PAHs in the gas phase. In contrast, the experimental band positions in the top panel of Figure 6 are solid-phase values with potential interactions with the TiO$_2$ surfaces. This difference can potentially explain the variations in band position between the solid phase experiments and the theoretical, gas phase, values. Nevertheless, theoretical spectra provide a good indication of the overall shape and intensities of the aliphatic C-H stretching bands making the identification of the experimental bands possible. To assign the experimental bands, the theoretical spectra of the hydrogenation products were compared one by one to the experimental spectra. Rather than fitting band by band, comparisons were made by taking into account the overall spectra profiles of the theoretical and experimental spectra.

The most intense experimental bands centered at 2960, 2932, and 2861 cm^{-1}, and the shoulder at 2907 cm^{-1} can be reproduced by hydrogenation products F_n, G_n, and H_n (see Figure 6 and Table S1), indicating the formation of peripherally hydrogenated naphthalene molecules (hydrogen atoms added to peripheral carbons) and fully hydrogenated molecules (hydrogen atoms added to all the carbons in the PAH). Products B_n and C_n are required to reproduce the shoulders centered at 2825 (theoretical values of 2807 and 2798 cm^{-1}) and 2843 cm^{-1} (theoretical values of 2833 and 2831 cm^{-1}), respectively, since those hydrogenation products are the only ones showing bands below 2850 cm^{-1}. Products D_n and E_n produce a band close to 2871 cm^{-1} (theoretical values of 2878 cm^{-1} for product D_n and 2880 cm^{-1} for product E_n). Based on Table S1, the band at 2960 cm^{-1} can be assigned to antisymmetric aliphatic C-H stretching modes from hydrogenated molecules, the bands around at 2932 cm^{-1} are produce by antisymmetric and symmetric aliphatic C-H stretching modes, and the bands around 2861 cm^{-1} are considered to be symmetric aliphatic C-H stretching modes.

The degree of hydrogenation can be determined using Figure 6. Full hydrogenation produces intense aliphatic bands around 2960 cm^{-1} and between 2930 to 2900 cm^{-1}. Complete peripheral hydrogenation of one or two rings of the naphthalene molecule produces bands between 2950 and 2850 cm^{-1}, as evidenced by product E_n and F_n. When the peripheral hydrogenation is only partial (products B_n and C_n), aliphatic bands are present bellow 2850 cm^{-1}. However, hydrogenation products B_n and C_n contain one unpaired electron making them more susceptible

16

to react with neighboring atoms and molecules. These hydrogenation products could bond to vacancies at the TiO_2 surface. This is explained in more detail in the discussion section.
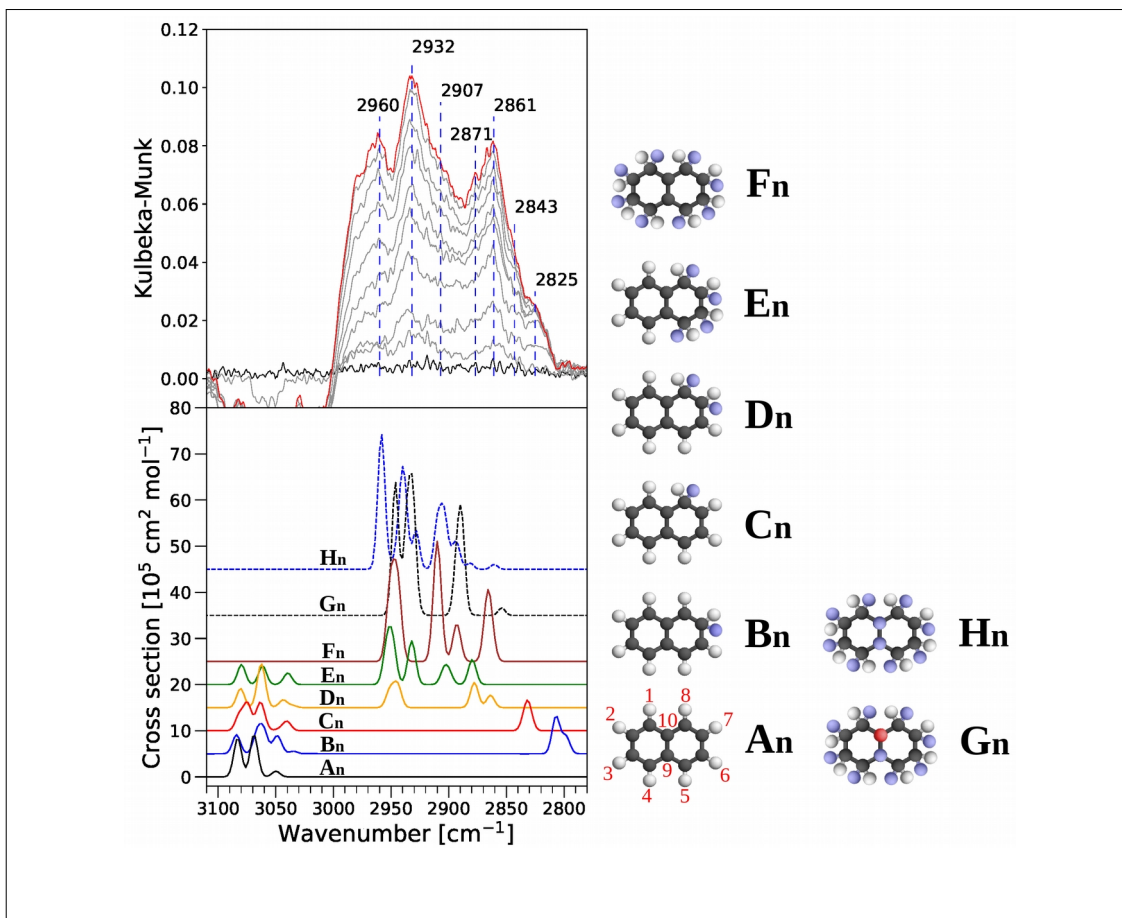

Figure 6. Top panel: Subtraction spectra of the naphthalene and TiO_2 mixture experiments. The IR data was collected over 24 hours at 10 minutes intervals. The black spectrum marks the beginning of the experiment, while the red spectrum marks the end. The gray spectra are selected measurements in between. Dashed vertical blue lines mark the new bands detected. Bottom panel: Theoretical spectra of the different hydrogenation products of naphthalene, partially, peripheral, and fully hydrogenated,

taken from the PAHdb database. Each hydrogenation product is marked with a letter that illustrates the corresponding molecular structure drawn on the right. Hydrogen positions for naphthalene are numbered in drawing A_n in red. Original hydrogen atoms are white, while the hydrogenation atoms are colored in blue when above the plane of the PAH, and red when below the plane of the PAH.

Hydrogenation rates have been calculated for three degrees of hydrogenation: a partial hydrogenation involving the addition of only a few hydrogen atoms (products B_n, C_n, and D_n are used for this rate), partial hydrogenation caused by a higher number of hydrogen atoms including complete peripheral hydrogenation of one or two rings (products E_n and F_n are used for this rate), and full hydrogenation where all the carbon atoms have a hydrogen atom attached (products G_n and H_n are used for this rate). This provides upper and lower limits in the production of aliphatic compounds. The theoretical A-values (integrated cross-section column in Table S1) of the hydrogenation products mentioned above were added into a single A-value for each hydrogenation rate in the aliphatic region of 3000 to 2780 cm^{-1}. Integrating the aliphatic region in the experimental data, a hydrogenation rate of 1.6×10^{14} molecules cm^{-2} per minute was found for a partial hydrogenation, 5.8×10^{13} molecules cm^{-2} per minute for partial, including complete peripheral, hydrogenation, and 1.7×10^{13} molecules cm^{-2} per minute for full hydrogenation.

Anthracene hydrogenation

The top panel in Figure 7 shows the subtraction spectra of the anthracene and TiO_2 experiment. As in the previous section, the aromatic bands appear as "negative" absorbance because of both the loss of anthracene due to sublimation (as evidenced by Figure 3) and the hydrogenation of the PAH. The decreasing rate of anthracene calculated by integrating the experimental aromatic bands is 8.1×10^{12} molecules cm^{-2} per minute, using the anthracene A-values from Szczepanski and Vala[71]. In the case of anthracene mixed with KBr, the decreasing rate was 1.4×10^{14} molecules cm^{-2} per minute. Thus, anthracene on TiO_2 sublimates 17 times slower than anthracene on KBr, implying a significant interaction between TiO_2 and anthracene.

Focusing in on the C-H stretching region, new bands grow over time at 2978, 2962, 2929, and 2857 cm^{-1}, as well as shoulders at 2905, 2876, and 2835 cm^{-1} (see Figure 7). Figure 8 shows the spectrum of anthracene and TiO_2 mixture at time 0 minutes and 360 minutes, as well as the subtraction spectrum for the 3200 to 1000 cm^{-1} region. New bands grow in the aliphatic C-H stretching region (around 3000 to 2700 cm^{-1}) as well as in the aliphatic C-H bending region (between 1475 to 1350 cm^{-1}), indicating that hydrogenation is taking place. Recall that anthracene in KBr (Figure 3) did not show any change in the spectra over time, indicating that the newly observed bands are a product of anthracene molecules interacting with the surface of TiO_2 dust particles.

Table S2 shows the positions and strengths of the aliphatic bands in the different hydrogenation products of anthracene drawn in Figure 7. As discussed in the naphthalene experiment, the aliphatic bands depend on the number of hydrogen atoms involved in the

hydrogenation as well as the position they occupy in the molecule. The different hydrogenation products drawn in Figure 7 start with the solo (no adjacent hydrogen atoms) positions 9 and 10 being the first positions to be hydrogenated. These positions are preferred sites on the anthracene molecule, meaning they have the highest probability of being hydrogenated first. This characteristic is based on the molecule's enthalpy of formation[72,73]. The rest of the positions are then subsequently hydrogenated, starting from the ones next to positions 9 and 10, i.e., positions 1, 4, 5, and 8 in Figure 7.

Similarly to the naphthalene experiments, and base on Table S2, the band at 2978 and 2962 cm^{-1} are antisymmetric aliphatic C-H stretching modes, the bands around at 2932 cm^{-1} are antisymmetric and symmetric aliphatic C-H stretching modes, and the bands around 2861 cm^{-1} are symmetric aliphatic C-H stretching modes. The double peak centered at 2978 and 2962 cm^{-1}, the bands centered at 2929 and 2857 cm^{-1}, and the shoulder at 2905 cm^{-1} in the experimental spectra are representative of complete peripheral and fully hydrogenated anthracene molecules as evidenced by hydrogenation products E_a, H_a, I_a, J_a, K_a, L_a, M_a, and N_a, see Figure 7. Shoulders at 2876 and 2835 cm^{-1} can be reproduce by the partially hydrogenated products B_a, C_a, D_a, F_a, and G_a. It is worth noticing that like the previous experiments, the fully hydrogenated products present a blue shift compared to the partially hydrogenated products in Figure 7. There is a small feature at 2991 cm^{-1} that could indicate a band, but it is most likely an artifact caused by the subtraction of the aromatic bands.
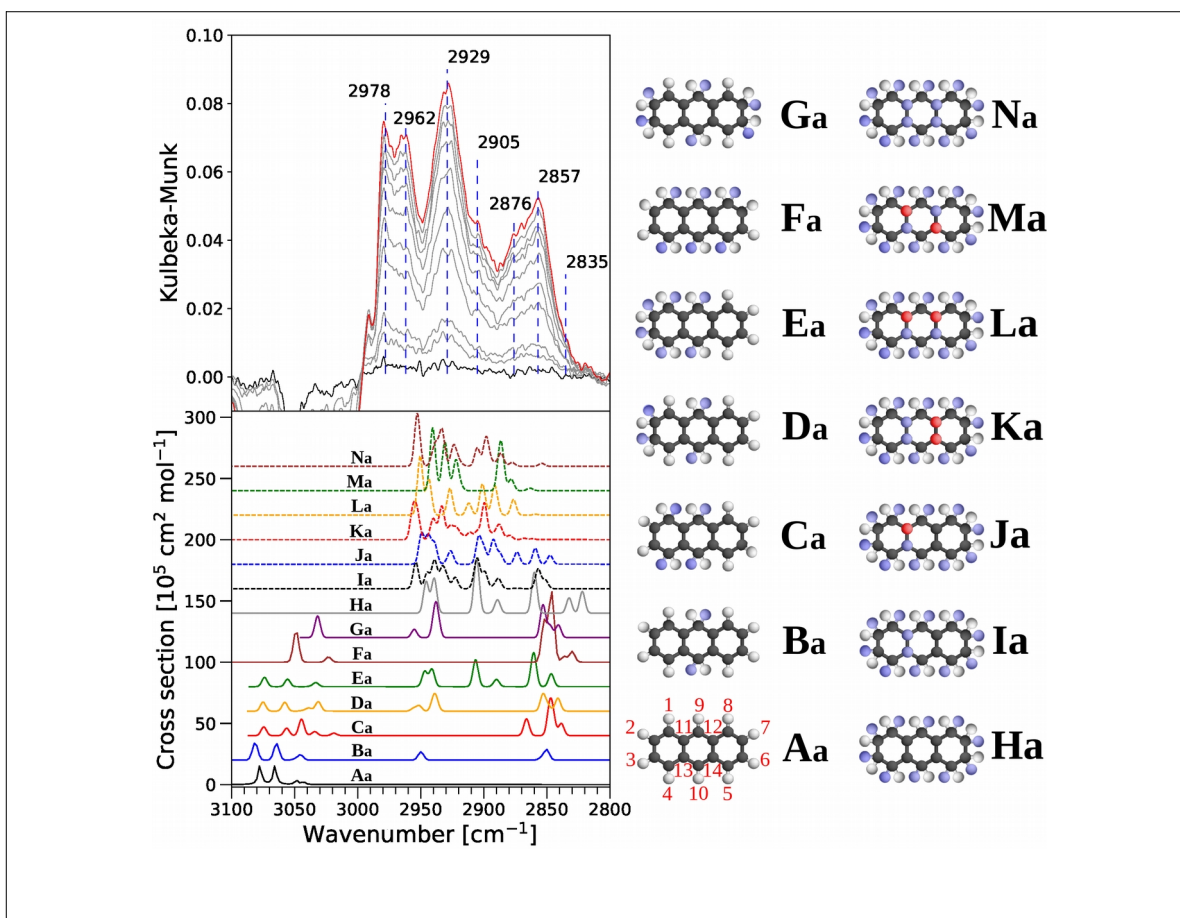
Figure 7. Top panel: Subtraction spectra of the anthracene and TiO$_2$ mixture experiments. The IR data was collected over 24 hours at 10 minutes intervals. The black spectrum marks the beginning of the experiment, while the red spectrum marks the end. The gray spectra are selected measurements in between. Dashed vertical blue lines mark the new bands detected. Bottom panel: Theoretical spectra of the different hydrogenation products of anthracene, partially, peripheral, and fully hydrogenated. Each hydrogenation product is marked with a letter corresponding to a molecular structure drawn on the right. Hydrogen positions for regular anthracene are numbered in drawing A$_a$ in red. Original hydrogen atoms are in white, additional hydrogenation atoms are colored in blue when above the

plane of the PAH, and red when below the plane of the PAH. The synthetic spectra for

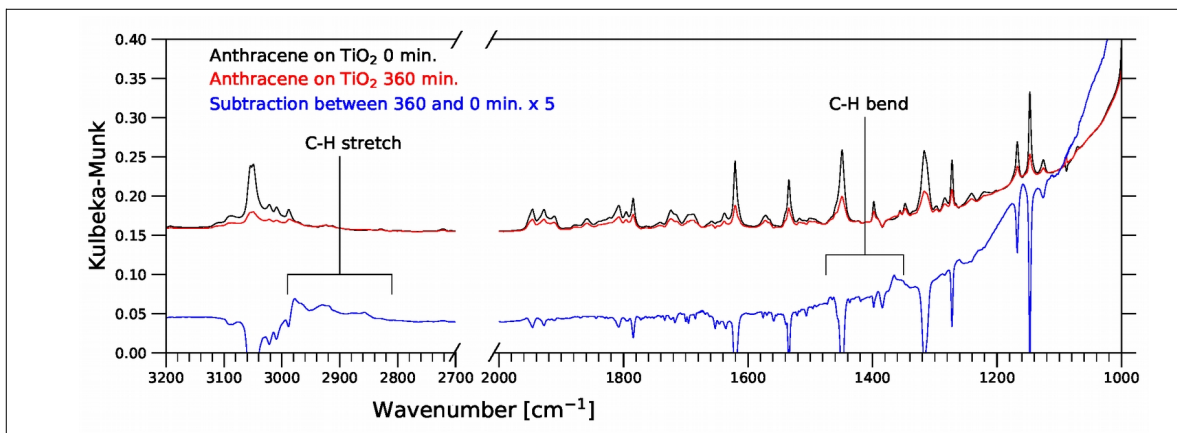anthracene products were calculated for this work using DFT calculations.

Figure 8. Anthracene mixed with TiO_2 at time 0 minutes (black) and after 360 minutes

(red). The blue spectrum is the subtraction between the spectra previously mentioned. The

subtraction spectrum was multiplied by 5 to highlight the new bands growing in the

aliphatic C-H stretching and bending regions marked by the dashed vertical lines.

As calculated for naphthalene, the hydrogenation rates were calculated using products B_a, C_a,

and D_a for a partial hydrogenation of the anthracene molecules by a few hydrogen atoms,

products E_a, F_a, G_a, H_a, I_a, and J_a where selected for a partial hydrogenation caused by a higher

number of hydrogen atoms including complete peripheral hydrogenation, and products K_a, L_a,

M_a, and N_a, where used for a full hydrogenation where all the carbon atoms are hydrogenated.

The theoretical A-values in Table S2 were added into a single A-value for each hydrogenation

rate in the aliphatic region of 3000 to 2800 cm^{-1}. Integrating the aliphatic bands in the

experimental data, a hydrogenation rate of 5.1×10^{13} molecules cm^{-2} per minute was calculated for

a partial hydrogenation, a hydrogenation rate of 8.2×10^{12} molecules cm^{-2} per minute for a partial

hydrogenation including complete peripheral hydrogenation, and a hydrogenation rate of

9.1×10^{12} molecules cm^{-2} per minute for a full hydrogenation.

Coronene hydrogenation

Two new bands can be observed growing in the aliphatic C-H stretching region at 2930 and

2822 cm^{-1} (see top panel of Figure 9). Because of their slow growth rate, spectra were acquired

every hour for coronene, versus every 10 minutes for naphthalene and anthracene. The new

bands are ten and eight times less intense than the ones detected in the naphthalene and

anthracene experiments, respectively, raising the question of whether aliphatic coronene bands

are intrinsically weaker than naphthalene and anthracene aliphatic C-H stretches or is this due to

a lower amount of hydrogenation. Table S3 shows the positions of the aliphatic bands in the

different hydrogenation products of coronene drawn in Figure 9 as well as their band strength.

Comparing the band strengths for product F_n in Table S1, product H_a in Table S2, and product F_c

in Table S3 (i.e., peripherally hydrogenated naphthalene, anthracene, and coronene), it is worth

noticing that the band strength values are generally on the same order of magnitude for the three

hydrogenation products. This similarity indicates that it is not an intrinsic issue but more likely a

lower degree of hydrogenation for the coronene molecule. Coronene is a compact molecule with

high thermodynamic stability. At equilibrium, there should be more aromatics than aliphatics

i.e., the equilibrium ratio K is less than one[74]. Thus, hydrogenation is unfavorable and the aliphatic band yield is expected to be low.

Focusing on the aliphatic C-H bending region, a weak band (less than 10% of the intensity of the band at 2929 cm^{-1}) was tentatively detected at 1365 cm^{-1}. Nevertheless, this band is close to noise level since it appears near the broad TiO_2 absorption band showed in Figure 5. Comparing experimental with theoretical spectra in Figure 9 and the band positions listed in Table S3, it can be noted that all coronene hydrogenation products but E_c and G_c, present bands close to the two new bands in the experimental data as product E_c does not have active antisymmetric bands, and product G_c bands are closer to the 2930 cm^{-1} band. The lack of antisymmetric features in product E_c is due to the high molecular symmetry of its planar structure. Hydrogen atoms have been added at positions 2, 3, 8, and 9 but, since a carbon atom separates those positions, the E_c molecule is planar and symmetric. For product E_c, its antisymmetric modes are inactive as they do not produce a change in the dipole moment of the coronene molecule. (see reference [75] for a more detailed explanation).

Symmetric stretches require lower energy (the antisymmetric stretches will always occur at the higher wavenumbers) than asymmetric stretches. Thus the band centered at 2930 cm^{-1} can be assigned to antisymmetric C-H stretching modes while the band 2822 cm^{-1} can be assigned to symmetric C-H stretching modes, see Figure 9 and Table S3. In the case of the 2930 cm^{-1} band, hydrogenation products D_c and F_c present antisymmetric modes closer to the experimental data. The same case for the 2822 cm^{-1} band, where the symmetric modes of products D_c and F_c are

more in line with the experiments. However, comparing the two experimental bands shows that the 2822 cm^{-1} band is broader and more intense than the 2930 cm^{-1} band. Additionally, this broad band could be produced by three bands centered at 2827, 2822, and 2810 cm^{-1}, see Figure 9. This suggests that product D_c is the strongest candidate in the identification of the coronene hydrogenation pattern because the symmetric modes of product D_c resemble this broad and more intense characteristic the 2822 cm^{-1} band present. Overall, coronene molecules are preferably partially hydrogenated with only a few hydrogen atoms added, explaining the observed low hydrogenation yield of coronene molecules in the presence of TiO_2. Hydrogenation of coronene follows the pattern in product D_c, where hydrogenation positions are subsequently filled one by one alongside each other. However, product D_c contains one unpaired electron, like the hydrogenation products B_n and C_n mentioned in the naphthalene section. D_c is more susceptible to react. Thus, it should be attached to a vacancy site (see discussion section). Besides proving that coronene is partially hydrogenated, product G_c (fully hydrogenated coronene) in Figure 9 presents the same pattern seen in the naphthalene and anthracene experiments. Fully hydrogenated bands are blue shifted compared with the partial hydrogenation of the PAH.

In this case, coronene is partially hydrogenated which means the hydrogenation rates are calculated for partial hydrogenation of the coronene molecules (products B_c, C_c, D_c were used for this rate) and complete peripheral hydrogenation (product F_c was used for this rate). The theoretical A-values in Table S3 were added into a single A-value for each hydrogenation rate in the aliphatic region of 2970 to 2760 cm^{-1}. Integrating the aliphatic bands in the experimental

data, a hydrogenation rate of 1.7×10^{12} molecules cm^{-2} per minute was calculated for partial hydrogenation and a rate of 1.8×10^{12} molecules cm^{-2} per minute for a complete peripheral hydrogenation.
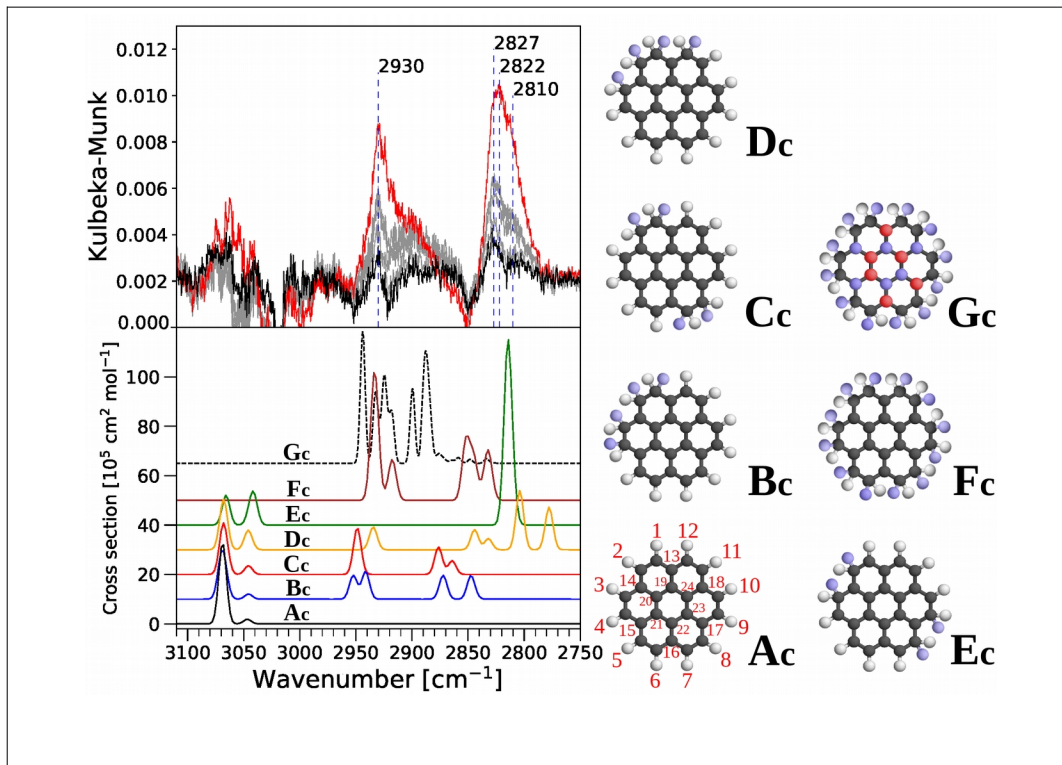

Figure 9. Top panel: Subtraction spectra of the coronene and TiO_2 mixture experiments. Data was collected over 24 hours taking a spectrum every hour. The black spectrum marks the beginning of the experiment, while the red spectrum marks the end. The gray spectra are selected measurements in between. The spectra has been baseline corrected. Bottom panel: Theoretical spectra of the different hydrogenation products of coronene, partially and peripherally hydrogenated, taken from the PAHdb database. The synthetic spectra for fully

hydrogenated coronene was calculated for this work using DFT calculations. Each hydrogenation product is marked with a letter corresponding to the molecular structure drawn on the right. Hydrogen positions for coronene are numbered in drawing A_c in red. Original hydrogen atoms are white, hydrogenation atoms are colored in blue when above the plane of the PAH, and red when below the plane of the PAH.

To summarize the results, based on the naphthalene and anthracene experiments, linear PAHs present similar hydrogenation patterns. The hydrogenation ranges from partial hydrogenation to full hydrogenation of the PAH. Full hydrogenation produces aliphatic bands at higher frequencies than partial hydrogenation. Thus, bands detected around 2960 cm^{-1} and above are an indication of a full hydrogenation of the PAH while bands around 2850 cm^{-1} and bellow indicate a partial hydrogenation, as evidenced by Figure 6, 7, and 9, and correlation plots in Figures S1, S2, and S3. The hydrogenation rate also changes depending on the molecule size. Naphthalene, the smallest PAH studied, exhibits the quickest hydrogenation followed by anthracene, and then coronene, the largest, which exhibits the slowest hydrogenation rate and does not undergo a complete hydrogenation.

DISCUSSION

Here we report on the catalytic hydrogenation of PAHs on TiO_2 dust grain surfaces under vacuum conditions without needing an external energy source or gas flow. Past studies focused on the degradation of PAHs through catalytic hydrogenation for environmental purposes because of the molecules' carcinogenic nature. Those experiments were performed in the presence of a heating source (raising the temperature higher than room temperature) and several atmospheres of H_2 and CO_2 gases[76–82].

Hydrogenation in our experiments can be explained by the Horiuti–Polanyi mechanism[83], which has been widely used to explain hydrogenation reactions. It is based on the dissociation of molecular hydrogen (generating an abundance of hydrogen atoms), followed by the addition of these hydrogen atoms to unsaturated molecules like PAHs.

In our experiments, H_2 is not used to hydrogenate PAHs. However, water molecules are chemisorbed on the TiO_2 surface. Solid TiO_2 is arranged with a lattice containing Ti ions (Ti_{5c}) and so-called bridging oxygen ions (O_b in Figure 10). However, defects in the lattice generate an absence of O_b atoms producing a vacancy (VO) site, see the top left panel in Figure 10. It is in this VO sites where water molecules can be dissociated. At room temperature, water molecules have enough thermal mobility to reach those sites. Once water molecules reach the grain surface, two distinct hydroxyl molecules can be formed: one as a terminal hydroxyl at the Ti site (OH-Ti_{5c}) and the other as a bridging hydroxyl (H-O_b), see top right panel in Figure 10[84–87]. After this catalytic dissociation, there would be a hydrogen pool available to react with the PAH molecules. The mobility of these hydrogen atoms is governed by thermal diffusion at room temperature.

TiO_2 anatase and rutile are used for catalysis purposes. Both forms present vacancies in their structures, but in the case of anatase, the vacancies are located in the subsurface and bulk while in rutile, they remain on the surface[88–90]. Figure 10 is an example of what could happen on the surface of TiO_2 grains. Nevertheless, the TiO_2 sample could present complex surfaces because of the grinding of the material, making the hydrogenation process more complex than the simplified version in Figure 10.

PAH molecules need to be adsorbed on the surface of the dust particle to be hydrogenated. This surface absorption can occur by chemisorption in which the PAH's C=C bonds rehybridize to form two metal-carbon covalent bonds or by physisorption occurring via weak π bonds with a minimum rearrangement of the molecular electronic density distribution[91]. The assumption of Horiuti-Polanyi mechanism, as responsible for the PAH hydrogenation on the surface of dust particles, implies that the hydrogen on the dust surfaces will react with the σ bonded PAHs. An external hydrogen atom induces a local sp^2 to sp^3 transition, breaking the PAH molecule's aromaticity. This addition delocalizes the positive charge in the π bond, making the PAH more reactive[92,93]. After adsorption, the unsaturated bonds of the reactant molecule (in our case PAHs) can incorporate those hydrogen atoms in a step-wise manner, forming half-hydrogenated intermediate species along the way, see Figure 10.

The presence of water molecules on the surface of TiO_2 grains is confirmed by a close up of the TiO_2 spectrum (see Figure 11) that shows the water bands at 3300 and 1650 cm^{-1}. After integrating the water O-H stretching mode centered at 3300 cm^{-1} and using the water band

strength from Hudgins et al.[94] we estimate that a total of 2.3×10^{15} molecules cm^{-2} are adsorbed on the TiO_2 surface.
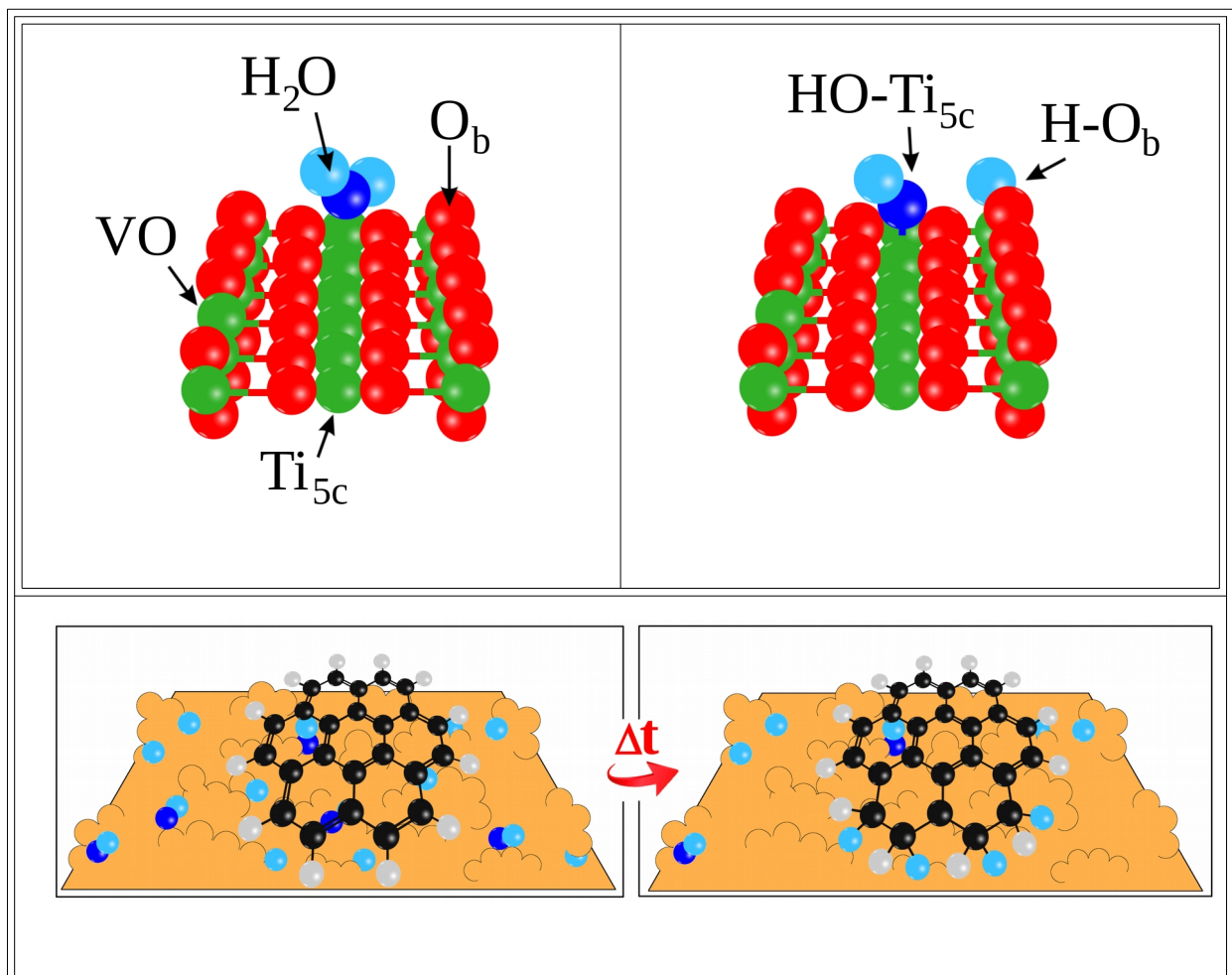

Figure 10. Top left, adsorption of water on the surface of TiO_2. Top right, dissociation of the water molecule where a hydrogen atom has been donated to the bridging O atom (O_b). A vacancy (VO) is also indicated, water molecules dissociate in such vacancies forming one H-O_b and one HO-Ti_{5c} molecule. Bottom, hydrogenation of coronene on TiO_2 (yellow background) over time. OH molecules are represented by connected blue (O) and light-blue

(H) balls. Hydrogen atoms are represented by light-blue balls to differentiate them from the

hydrogen in the coronene molecule. The yellow substrate represents TiO_2 powder.
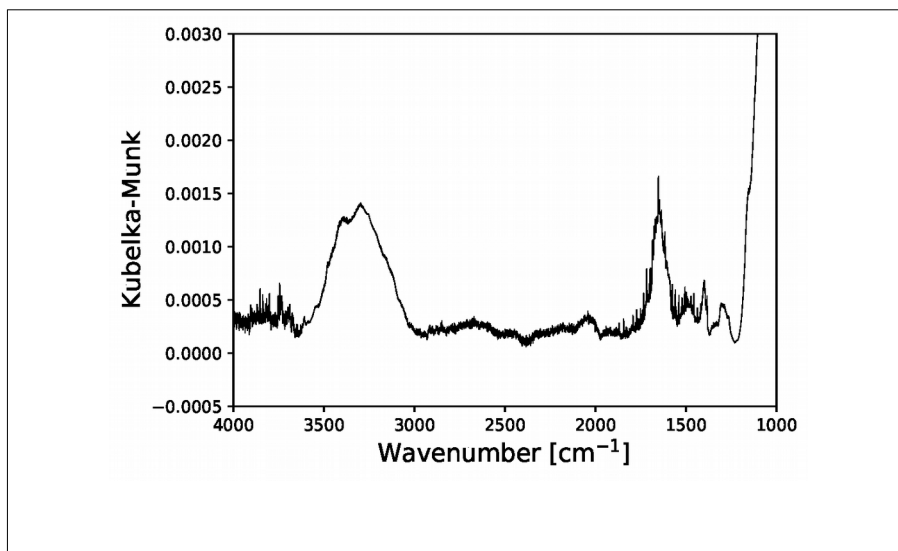

Figure 11. Close up of the TiO_2 spectrum. The strong absorption

starting at 1200 cm^{-1} belongs to the TiO_2. Water spectral bands are

detected at 3300 cm^{-1} (O-H stretching with an intensity of 0.0014 in

Kulbeka-Monk units) and 1650 cm^{-1} (O-H bending with an intensity

of 0.0013 in Kulbeka-Monk units) proving the presence of water

molecules on the grain surface.

PAHs are effectively hydrogenated when in contact with grain surfaces as evidenced by

Figures 6, 7, and 9. The hydrogenation can be partial (a few hydrogen atoms attached to the

PAH), peripheral (hydrogenation on the outside of the rings), and full (all carbon atoms in the

PAH have a hydrogen atom attached). Figure 12 shows the naphthalene, anthracene, and coronene spectrum after 24 hours of hydrogenation. When comparing the experimental data, it is easy to see that naphthalene aliphatic bands fall in the same region as anthracene aliphatic bands. Their asymmetric C-H stretching modes fall around 2970 cm^{-1}, the symmetric C-H stretching modes are around 2860 cm^{-1}, and a combination of antisymmetric and symmetric modes are present around 2930 cm^{-1}, see Tables S1 and S2. All the aliphatic modes fall in the same region as naphthalene and anthracene are small linear PAHs that present a similar hydrogenation process, where peripheral and fully hydrogenation is preferred. Nevertheless, some differences between the two-hydrogenation processes can be found. Anthracene presents a double peak at 2978 and 2962 cm^{-1} while naphthalene has one broad band at 2960 cm^{-1}. Naphthalene has a small band at 2825 cm^{-1} that does not seem to appear in the anthracene spectrum. However, this small band is the most intense feature in coronene, a partially hydrogenated PAH.
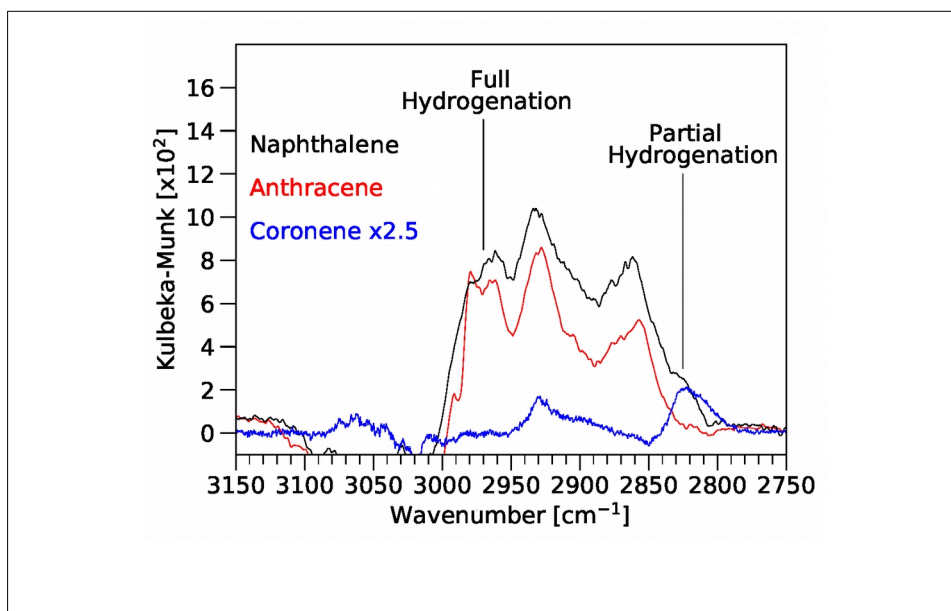
Figure 12. Naphthalene (black), anthracene (red), and coronene (blue) on TiO$_2$ after 24 hours. Coronene spectrum has been multiplied by a factor of 2.5 to match the shoulder at 2825 cm^{-1} in the naphthalene spectrum.

It is important to recall that fully hydrogenated bands are blue shifted compared to partial hydrogenated bands, see Figures 6, 7, and 9. Based on this effect, and the experimental features mentioned above, it is safe to argue that the dominant hydrogenated product in the anthracene experiment is fully hydrogenated anthracene. The lack of the 2825 cm^{-1} band and the peak at 2978 cm^{-1} in the anthracene spectrum could be an indication of fully hydrogenated anthracene molecules. Naphthalene undergoes a full hydrogenation process resembling the hydrogenation process of anthracene but partially hydrogenated naphthalene is still present, as evidenced by the shoulder at 2825 cm^{-1}. Unlike the other two PAHs, coronene presents only a partial hydrogenation where the band at 2825 cm^{-1} is stronger than the one at 2930 cm^{-1}. However, this partial hydrogenation is not random since neighboring carbon atoms in coronene have to be hydrogenated sequentially, as evidence by product D$_c$ in Figure 9. The hydrogenation rates of the PAHs appear to be size dependent, with naphthalene hydrogenation occurring at the fastest rate and coronene the slowest, see Table 1.

Table 1. Upper and lower hydrogenation production rates for naphthalene, anthracene, and coronene calculated for three different scenarios.

	Hydrogenation production rate [molecules cm^{-2} $minute^{-1}$]		
PAH	**Case 1[a]**	**Case 2[b]**	**Case 3[c]**
Naphthalene	$1.6x10^{14}$	$5.8x10^{13}$	$1.7x10^{13}$
Anthracene	$5.1x10^{13}$	$8.1x10^{12}$	$9.1x10^{12}$
Coronene	$1.7x10^{12}$	$1.8x10^{12}$	-

a) Partial hydrogenation where a few hydrogen atoms are attached to the PAH. b) Partial hydrogenation caused by a higher number of hydrogen molecules attached to the PAH including complete hydrogenation of rings. c) Full hydrogenation where all the carbon atoms have a hydrogen atom attached.

CONCLUSION

In this work we have presented experimental and theoretical results on the catalytic hydrogenation of PAH molecules on the surface of dust particles under vacuum conditions. Three different PAH samples (naphthalene, anthracene, and coronene), mixed with titanium dioxide powder, were analyzed using DRIFTS. New bands, growing as a function of time, were detected in all three samples in the aliphatic C-H stretching region, and with the help of theoretical calculations, the experimental spectra were interpreted and bands were assigned to antisymmetric and symmetric aliphatic C-H modes of various hydrogenation products.

PAHs studied here present different hydrogenation processes, anthracene molecules undergo a fully hydrogenation of the anthracene molecule, naphthalene molecules are fully hydrogenated as well but some partial hydrogenated molecules remained, and coronene can only be partially hydrogenated. In the case of coronene, its hydrogenation is sequential. Bands detected around and above 2960 cm^{-1} are an indication of a full hydrogenation of the PAH while bands around and bellow 2850 cm^{-1} indicate a partial hydrogenation. The carbon atoms are subsequently filled one by one alongside each other. The hydrogenation production rate depends on the size of the PAH, the smaller the higher its hydrogenation rate will be.

AUTHOR INFORMATION

Corresponding Author

*Email: gustavo.a.cruzdiaz@nasa.gov

ORCID iD: 0000-0003-2270-6103

Author Contributions

The manuscript was written through contributions of all authors. All authors have given approval to the final version of the manuscript. +, §, ǂ These authors contributed equally.

Supporting Information

As supporting information, we provide Tables S1, S2, and S3. These are theoretical aliphatic band positions and intensities, taken from the PAHdb database for naphthalene and coronene, and computed for the hydrogenated anthracene products. The hydrogenation positions involved in the CH_2 stretching modes are given as well.

REFERENCES

(1) Peeters, E.; Hony, S.; Kerckhoven, C. V.; Tielens, A. G. G. M.; Allamandola, L. J.; Hudgins, D. M.; Bauschlicher, C. W. The Rich 6 to 9 m Spectrum of Interstellar PAHs. *A&A* **2002**, *390* (3), 1089–1113. https://doi.org/10.1051/0004-6361:20020773.

(2) Peeters, E.; Mattioda, A. L.; Hudgins, D. M.; Allamandola, L. J. Polycyclic Aromatic Hydrocarbon Emission in the 15-21 Micron Region. *ApJ* **2004**, *617* (1), L65–L68. https://doi.org/10.1086/427186.

(3) Peeters, E.; Tielens, A. G. G. M.; Allamandola, L. J.; Wolfire, M. G. THE 15–20 micron EMISSION IN THE REFLECTION NEBULA NGC 2023. *ApJ* **2012**, *747* (1), 44, 1-11. https://doi.org/10.1088/0004-637X/747/1/44.

(4) Habart, E.; Natta, A.; Krügel, E. PAHs in Circumstellar Disks around Herbig Ae/Be Stars. *A&A* **2004**, *427* (1), 179–192. https://doi.org/10.1051/0004-6361:20035916.

(5) Cami, J.; Bernard-Salas, J.; Peeters, E.; Malek, S. E. Detection of C60 and C70 in a Young Planetary Nebula. *Science* **2010**, *329* (5996), 1180–1182. https://doi.org/10.1126/science.1192035.

(6) Gredel, R.; Carpentier, Y.; Rouillé, G.; Steglich, M.; Huisken, F.; Henning, T. Abundances of PAHs in the ISM: Confronting Observations with Experimental Results. *A&A* **2011**, *530*, A26-A41. https://doi.org/10.1051/0004-6361/201116602.

(7) Salama, F.; Galazutdinov, G. A.; Kre\lowski, J.; Biennier, L.; Beletsky, Y.; Song, I.-O. POLYCYCLIC AROMATIC HYDROCARBONS AND THE DIFFUSE INTERSTELLAR BANDS: A SURVEY. *ApJ* **2011**, *728* (2), 154, 1-8. https://doi.org/10.1088/0004-637X/728/2/154.

(8) Geers, V. C.; Augereau, J.-C.; Pontoppidan, K. M.; Dullemond, C. P.; Visser, R.; Kessler-Silacci, J. E.; Evans, N. J.; Dishoeck, E. F. van; Blake, G. A.; Boogert, A. C. A.; Brown, J. M.; Lahuis, F.; Merín, B. C2D Spitzer-IRS Spectra of Disks around T Tauri Stars - II. PAH Emission Features. *A&A* **2006**, *459* (2), 545–556. https://doi.org/10.1051/0004-6361:20064830.

(9) Acke, B.; Ancker, M. E. van den; Dullemond, C. P.; Boekel, R. van; Waters, L. B. F. M. Correlation between Grain Growth and Disk Geometry in Herbig Ae/Be Systems. *A&A* **2004**, *422* (2), 621–626. https://doi.org/10.1051/0004-6361:20040197.

(10) Meeus, G.; Waters, L. B. F. M.; Bouwman, J.; Ancker, M. E. van den; Waelkens, C.; Malfait, K. ISO Spectroscopy of Circumstellar Dust in 14 Herbig Ae/Be Systems: Towards an Understanding of Dust Processing. *A&A* **2001**, *365* (3), 476–490. https://doi.org/10.1051/0004-6361:20000144.

(11) Acke, B.; Ancker, M. E. van den. A Survey for Nanodiamond Features in the 3 Micron Spectra of Herbig Ae/Be Stars. *A&A* **2006**, *457* (1), 171–181. https://doi.org/10.1051/0004-6361:20065612.

(12) Geers, V. C.; Dishoeck, E. F. van; Visser, R.; Pontoppidan, K. M.; Augereau, J.-C.; Habart, E.; Lagrange, A. M. Spatially Extended Polycyclic Aromatic Hydrocarbons in Circumstellar Disks around T Tauri and Herbig Ae Stars. *A&A* **2007**, *476* (1), 279–289. https://doi.org/10.1051/0004-6361:20078466.

(13) Doucet, C.; Habart, E.; Pantin, E.; Dullemond, C.; Lagage, P. O.; Pinte, C.; Duchêne, G.; Ménard, F. HD 97048: A Closer Look at the Disk. *A&A* **2007**, *470* (2), 625–631. https://doi.org/10.1051/0004-6361:20066610.

(14) Wing, M. R.; Bada, J. L. The Origin of the Polycyclic Aromatic Hydrocarbons in Meteorites. *Origins Life Evol Biosphere* **1991**, *21* (5), 375–383. https://doi.org/10.1007/BF01808308.

(15) Cronin, J. R.; Pizzarello, S.; Epstein, S.; Krishnamurthy, R. V. Molecular and Isotopic Analyses of the Hydroxy Acids, Dicarboxylic Acids, and Hydroxydicarboxylic Acids of the Murchison Meteorite. *Geochimica et Cosmochimica Acta* **1993**, *57* (19), 4745–4752. https://doi.org/10.1016/0016-7037(93)90197-5.

(16) Becker, L.; Glavin, D. P.; Bada, J. L. Polycyclic Aromatic Hydrocarbons (PAHs) in Antarctic Martian Meteorites, Carbonaceous Chondrites, and Polar Ice. *Geochimica et*

Cosmochimica Acta **1997**, *61* (2), 475–481. https://doi.org/10.1016/S0016-7037(96)00400-0.

(17) Sabbah, H.; Morrow, A. L.; Jenniskens, P.; Shaddad, M. H.; Zare, R. N. Polycyclic Aromatic Hydrocarbons in Asteroid 2008 TC3: Dispersion of Organic Compounds inside Asteroids. *Meteoritics & Planetary Science* **2010**, *45* (10–11), 1710–1717. https://doi.org/10.1111/j.1945-5100.2010.01103.x.

(18) Campins, H.; Hargrove, K.; Pinilla-Alonso, N.; Howell, E. S.; Kelley, M. S.; Licandro, J.; Mothé-Diniz, T.; Fernández, Y.; Ziffer, J. Water Ice and Organics on the Surface of the Asteroid 24 Themis. *Nature* **2010**, *464* (7293), 1320–1321. https://doi.org/10.1038/nature09029.

(19) Rivkin, A. S.; Emery, J. P. Detection of Ice and Organics on an Asteroidal Surface. *Nature* **2010**, *464* (7293), 1322–1323. https://doi.org/10.1038/nature09028.

(20) Li, A. PAHs in Comets: An Overview. In *Deep Impact as a World Observatory Event: Synergies in Space, Time, and Wavelength*; Käufl, H. U., Sterken, C., Eds.; Eso Astrophysics Symposia; Springer: Berlin, Heidelberg, 2009; pp 161–175. https://doi.org/10.1007/978-3-540-76959-0_21.

(21) Sandford, S. A.; Aléon, J.; Alexander, C. M. O.; Araki, T.; Bajt, S.; Baratta, G. A.; Borg, J.; Bradley, J. P.; Brownlee, D. E.; Brucato, J. R.; Burchell, M. J.; Busemann, H.; Butterworth, A.; Clemett, S. J.; Cody, G.; Colangeli, L.; Cooper, G.; D'Hendecourt, L.; Djouadi, Z.; Dworkin, J. P.; Ferrini, G.; Fleckenstein, H.; Flynn, G. J.; Franchi, I. A.; Fries, M.; Gilles, M. K.; Glavin, D. P.; Gounelle, M.; Grossemy, F.; Jacobsen, C.; Keller, L. P.; Kilcoyne, A. L. D.; Leitner, J.; Matrajt, G.; Meibom, A.; Mennella, V.; Mostefaoui, S.; Nittler, L. R.; Palumbo, M. E.; Papanastassiou, D. A.; Robert, F.; Rotundi, A.; Snead, C. J.; Spencer, M. K.; Stadermann, F. J.; Steele, A.; Stephan, T.; Tsou, P.; Tyliszczak, T.; Westphal, A. J.; Wirick, S.; Wopenka, B.; Yabuta, H.; Zare, R. N.; Zolensky, M. E. Organics Captured from Comet 81P/Wild 2 by the Stardust Spacecraft. *Science* **2006**, *314* (5806), 1720–1724. https://doi.org/10.1126/science.1135841.

(22) Cruikshank, D. P.; Wegryn, E.; Dalle Ore, C. M.; Brown, R. H.; Bibring, J.-P.; Buratti, B. J.; Clark, R. N.; McCord, T. B.; Nicholson, P. D.; Pendleton, Y. J.; Owen, T. C.; Filacchione, G.; Coradini, A.; Cerroni, P.; Capaccioni, F.; Jaumann, R.; Nelson, R. M.; Baines, K. H.; Sotin, C.; Bellucci, G.; Combes, M.; Langevin, Y.; Sicardy, B.; Matson, D. L.; Formisano, V.; Drossart, P.; Mennella, V. Hydrocarbons on Saturn's Satellites Iapetus and Phoebe. *Icarus* **2008**, *193* (2), 334–343. https://doi.org/10.1016/j.icarus.2007.04.036.

(23) Mennella, V.; Hornekær, L.; Thrower, J.; Accolla, M. THE CATALYTIC ROLE OF CORONENE FOR MOLECULAR HYDROGEN FORMATION. *ApJL* **2011**, *745* (1), L2-L7. https://doi.org/10.1088/2041-8205/745/1/L2.

(24) Thrower, J. D.; Jørgensen, B.; Friis, E. E.; Baouche, S.; Mennella, V.; Luntz, A. C.; Andersen, M.; Hammer, B.; Hornekær, L. EXPERIMENTAL EVIDENCE FOR THE FORMATION OF HIGHLY SUPERHYDROGENATED POLYCYCLIC AROMATIC

HYDROCARBONS THROUGH H ATOM ADDITION AND THEIR CATALYTIC ROLE IN H2FORMATION. *ApJ* **2012**, *752* (1), 3, 1-6. https://doi.org/10.1088/0004-637X/752/1/3.

(25) Ferullo, R. M.; Zubieta, C. E.; Belelli, P. G. Hydrogenated Polycyclic Aromatic Hydrocarbons (HnPAHs) as Catalysts for Hydrogenation Reactions in the Interstellar Medium: A Quantum Chemical Model. *Phys. Chem. Chem. Phys.* **2019**, *21* (22), 12012–12020. https://doi.org/10.1039/C9CP02329A.

(26) Cazaux, S.; Boschman, L.; Rougeau, N.; Reitsma, G.; Hoekstra, R.; Teillet-Billy, D.; Morisset, S.; Spaans, M.; Schlathölter, T. The Sequence to Hydrogenate Coronene Cations: A Journey Guided by Magic Numbers. *Scientific Reports* **2016**, *6* (1), 19835, 1-7. https://doi.org/10.1038/srep19835.

(27) Cazaux, S.; Arribard, Y.; Egorov, D.; Palotás, J.; Hoekstra, R.; Berden, G.; Oomens, J.; Schlathölter, T. The Sequence of Coronene Hydrogenation Revealed by Gas-Phase IR Spectroscopy. *ApJ* **2019**, *875* (1), 27, 1-8. https://doi.org/10.3847/1538-4357/ab0e01.

(28) Allamandola, L. J.; Bregman, J. D.; Sandford, S. A.; Tielens, A. G. G. M.; Witteborn, F. C.; Wooden, D. H.; Rank, D. The Discovery of a New Infrared Emission Feature at 1905 Wavenumbers (5.25 Microns) in the Spectrum of BD + 30 Deg 3639 and Its Relation to the Polycyclic Aromatic Hydrocarbon Model. *The Astrophysical Journal Letters* **1989**, *345*, L59–L62. https://doi.org/10.1086/185552.

(29) Allamandola, L. J.; Tielens, A. G. G. M.; Barker, J. R. Interstellar Polycyclic Aromatic Hydrocarbons - The Infrared Emission Bands, the Excitation/Emission Mechanism, and the Astrophysical Implications. *The Astrophysical Journal Supplement Series* **1989**, *71*, 733–775. https://doi.org/10.1086/191396.

(30) Allamandola, L. J.; Hudgins, D. M.; Sandford, S. A. Modeling the Unidentified Infrared Emission with Combinations of Polycyclic Aromatic Hydrocarbons. *The Astrophysical Journal Letters* **1999**, *511*, L115–L119. https://doi.org/10.1086/311843.

(31) Tielens, A. G. G. M. Interstellar Polycyclic Aromatic Hydrocarbon Molecules. *Annual Review of Astronomy and Astrophysics* **2008**, *46*, 289–337. https://doi.org/10.1146/annurev.astro.46.060407.145211.

(32) Bernstein, M. P.; Sandford, S. A.; Allamandola, L. J. Hydrogenated Polycyclic Aromatic Hydrocarbons and the 2940 and 2850 Wavenumber (3.40 and 3.51 Micron) Infrared Emission Features. *ApJ* **1996**, *472* (2), L127–L130. https://doi.org/10.1086/310376.

(33) Bernstein, M. P.; Sandford, S. A.; Allamandola, L. J.; Gillette, J. S.; Clemett, S. J.; Zare, R. N. UV Irradiation of Polycyclic Aromatic Hydrocarbons in Ices: Production of Alcohols, Quinones, and Ethers. *Science* **1999**, *283* (5405), 1135–1138. https://doi.org/10.1126/science.283.5405.1135.

(34) Bernstein, M. P.; Elsila, J. E.; Dworkin, J. P.; Sandford, S. A.; Allamandola, L. J.; Zare, R. N. Side Group Addition to the Polycyclic Aromatic Hydrocarbon Coronene by Ultraviolet

Photolysis in Cosmic Ice Analogs. *ApJ* **2002**, *576* (2), 1115–1120. https://doi.org/10.1086/341863.

(35) Sloan, G. C.; Bregman, J. D.; Geballe, T. R.; Allamandola, L. J.; Woodward, C. E. Variations in the 3 Micron Spectrum across the Orion Bar: Polycyclic Aromatic Hydrocarbons and Related Molecules. *Astrophys. J.* **1997**, *474* (2 Pt 1), 735–740. https://doi.org/10.1086/303484.

(36) Wagner, D. R.; Kim, H.; Saykally, R. J. Peripherally Hydrogenated Neutral Polycyclic Aromatic Hydrocarbons as Carriers of the 3 Micron Interstellar Infrared Emission Complex: Results from Single-Photon Infrared Emission Spectroscopy. *ApJ* **2000**, *545* (2), 854–860. https://doi.org/10.1086/317868.

(37) Sandford, S. A.; Bernstein, M. P.; Allamandola, L. J.; Gillette, J. S.; Zare, R. N. Deuterium Enrichment of Polycyclic Aromatic Hydrocarbons by Photochemically Induced Exchange with Deuterium-Rich Cosmic Ices. *Astrophys. J.* **2000**, *538* (2 Pt 1), 691–697. https://doi.org/10.1086/309147.

(38) Sandford, S. A.; Bernstein, M. P.; Materese, C. K. THE INFRARED SPECTRA OF POLYCYCLIC AROMATIC HYDROCARBONS WITH EXCESS PERIPHERAL H ATOMS (H n -PAHs) AND THEIR RELATION TO THE 3.4 AND 6.9 micron PAH EMISSION FEATURES. *ApJS* **2013**, *205* (1), 8, 1-30. https://doi.org/10.1088/0067-0049/205/1/8.

(39) Pauzat, F.; Ellinger, Y. The 3.2–3.5 Mm Region Revisited — II. A Theoretical Study of the Effects of Hydrogenation on Some Model PAHs. *Mon Not R Astron Soc* **2001**, *324* (2), 355–366. https://doi.org/10.1046/j.1365-8711.2001.04277.x.

(40) Steglich, M.; Jäger, C.; Huisken, F.; Friedrich, M.; Plass, W.; Räder, H.-J.; Müllen, K.; Henning, T. THE ABUNDANCES OF HYDROCARBON FUNCTIONAL GROUPS IN THE INTERSTELLAR MEDIUM INFERRED FROM LABORATORY SPECTRA OF HYDROGENATED AND METHYLATED POLYCYCLIC AROMATIC HYDROCARBONS. *ApJS* **2013**, *208* (2), 26, 1-22. https://doi.org/10.1088/0067-0049/208/2/26.

(41) Materese, C. K.; Bregman, J. D.; Sandford, S. A. The Detection of 6.9 Mm Emission Features in the Infrared Spectra of IRAS 04296+3429, IRAS 05341+0852, and IRAS 22272+5435: Evidence for the Presence of Hn-PAHs in Post-AGB Stars. *The Astrophysical Journal* **2017**, *850*, 165, 1-5. https://doi.org/10.3847/1538-4357/aa960d.

(42) J. Mackie, C.; Candian, A.; Huang, X.; Maltseva, E.; Petrignani, A.; Oomens, J.; Jan Buma, W.; J. Lee, T.; M. Tielens, A. G. G. The Anharmonic Quartic Force Field Infrared Spectra of Hydrogenated and Methylated PAHs. *Physical Chemistry Chemical Physics* **2018**, *20* (2), 1189–1197. https://doi.org/10.1039/C7CP06546A.

(43) Siebenmorgen, R.; Kruegel, E. Dust Model Containing Polycyclic Aromatic Hydrocarbons in Various Environments. *Astronomy and Astrophysics* **1992**, *259*, 614–626.

(44) Greenberg, J. M.; Shen, C. Cosmic Dust in The 21st Century. In *Toward a New Millennium in Galaxy Morphology*; Block, D. L., Puerari, I., Stockton, A., Ferreira, D., Eds.; Springer Netherlands: Dordrecht, 2000; pp 33–58. https://doi.org/10.1007/978-94-011-4114-7_3.

(45) Zubko, V.; Dwek, E.; Arendt, R. G. Interstellar Dust Models Consistent with Extinction, Emission, and Abundance Constraints. *ApJS* **2004**, *152* (2), 211–249. https://doi.org/10.1086/382351.

(46) Draine, B. T.; Li, A. Infrared Emission from Interstellar Dust. IV. The Silicate-Graphite-PAH Model in the Post-SpitzerEra. *ApJ* **2007**, *657* (2), 810–837. https://doi.org/10.1086/511055.

(47) Dwek, E.; Cherchneff, I. THE ORIGIN OF DUST IN THE EARLY UNIVERSE: PROBING THE STAR FORMATION HISTORY OF GALAXIES BY THEIR DUST CONTENT. *ApJ* **2011**, *727* (2), 63, 1-12. https://doi.org/10.1088/0004-637X/727/2/63.

(48) Bekki, K. Coevolution of Dust, Gas and Stars in Galaxies – I. Spatial Distributions and Scaling-Relations of Dust and Molecular Hydrogen. *Mon Not R Astron Soc* **2013**, *432* (3), 2298–2323. https://doi.org/10.1093/mnras/stt589.

(49) Zhao, T. Q.; Li, Q.; Liu, B. S.; Gover, R. K. E.; Sarre, P. J.; Cheung, A. S.-C. Laboratory Astrochemistry: Catalytic Conversion of Acetylene to Polycyclic Aromatic Hydrocarbons over SiC Grains. *Phys. Chem. Chem. Phys.* **2016**, *18* (5), 3489–3496. https://doi.org/10.1039/C5CP06425B.

(50) Haritash, A. K.; Kaushik, C. P. Biodegradation Aspects of Polycyclic Aromatic Hydrocarbons (PAHs): A Review. *Journal of Hazardous Materials* **2009**, *169* (1), 1–15. https://doi.org/10.1016/j.jhazmat.2009.03.137.

(51) Leng, Y.; Liu, J.; Jiang, P.; Wang, J. Organometallic-Polyoxometalate Hybrid Based on V-Schiff Base and Phosphovanadomolybdate as a Highly Effective Heterogenous Catalyst for Hydroxylation of Benzene. *Chemical Engineering Journal* **2014**, *239*, 1–7. https://doi.org/10.1016/j.cej.2013.10.092.

(52) Kraeutler, B.; Bard, A. J. Heterogeneous Photocatalytic Preparation of Supported Catalysts. Photodeposition of Platinum on Titanium Dioxide Powder and Other Substrates. *J. Am. Chem. Soc.* **1978**, *100* (13), 4317–4318. https://doi.org/10.1021/ja00481a059.

(53) Eschemann, T. O.; Bitter, J. H.; de Jong, K. P. Effects of Loading and Synthesis Method of Titania-Supported Cobalt Catalysts for Fischer–Tropsch Synthesis. *Catalysis Today* **2014**, *228*, 89–95. https://doi.org/10.1016/j.cattod.2013.10.041.

(54) Mason, B. Pyroxenes in Meteorites. *Lithos* **1968**, *1* (1), 1–11. https://doi.org/10.1016/S0024-4937(68)80030-1.

(55) Cruikshank, D. P.; Hartmann, W. K. The Meteorite-Asteroid Connection: Two Olivine-Rich Asteroids. *Science* **1984**, *223* (4633), 281–283. https://doi.org/10.1126/science.223.4633.281.

(56) Jeong, K. S.; Winters, J. M.; Bertre, T. L.; Sedlmayr, E. Self-Consistent Modeling of the Outflow from the O-Rich Mira IRC –20197. *A&A* **2003**, *407* (1), 191–206. https://doi.org/10.1051/0004-6361:20030693.

(57) Kamiński, T. Molecular Dust Precursors in Envelopes of Oxygen-Rich AGB Stars and Red Supergiants. *Proceedings of the International Astronomical Union* **2018**, *14* (S343), 108–118. https://doi.org/10.1017/S1743921318006038.

(58) Goumans, T. P. M.; Bromley, S. T. Stardust Silicate Nucleation Kick-Started by SiO+TiO2. *Philosophical Transactions of the Royal Society A: Mathematical, Physical and Engineering Sciences* **2013**, *371* (1994), 20110580, 1-11. https://doi.org/10.1098/rsta.2011.0580.

(59) Yang, D.; Li, Y.; Liu, X.; Cao, Y.; Gao, Y.; Shen, Y. R.; Liu, W.-T. Facet-Specific Interaction between Methanol and TiO $_2$ Probed by Sum-Frequency Vibrational Spectroscopy. *Proc Natl Acad Sci USA* **2018**, *115* (17), E3888–E3894. https://doi.org/10.1073/pnas.1802741115.

(60) Setvin, M.; Shi, X.; Hulva, J.; Simschitz, T.; Parkinson, G. S.; Schmid, M.; Di Valentin, C.; Selloni, A.; Diebold, U. Methanol on Anatase TiO $_2$ (101): Mechanistic Insights into Photocatalysis. *ACS Catal.* **2017**, *7* (10), 7081–7091. https://doi.org/10.1021/acscatal.7b02003.

(61) Armaroli, T.; Bécue, T.; Gautier, S. Diffuse Reflection Infrared Spectroscopy (Drifts): Application to the in Situ Analysis of Catalysts. *Oil & Gas Science and Technology - Rev. IFP* **2004**, *59* (2), 215–237. https://doi.org/10.2516/ogst:2004016.

(62) Frisch, M.J.; Trucks, G.W.; Schlegel, H.B.; Scuseria, G.E.; Robb, M.A.; Cheeseman, J.R.; Scalmani, G.; Barone, V.; Petersson, G.A.; Nakatsuji, H.; Li, X.; Caricato, M.; Marenich, A.V.; Bloino, J.; Janesko, B.G.; Gomperts, R.; Mennucci, B.; Hratchian, H.P.; Ortiz, J.V.; Izmaylov, A.F.; Sonnenberg, J.L.; Williams-Young, D.; Ding, F.; Lipparini, F.; Egidi, F.; Goings, J.; Peng, B.; Petrone, A.; Henderson, T.; Ranasinghe, D.; Zakrzewski, V.G.; Gao, J.; Rega, N.; Zheng, G.; Liang, W.; Hada, M.; Ehara, M.; Toyota, K.; Fukuda, R.; Hasegawa, J.; Ishida, M.; Nakajima, T.; Honda, Y.; Kitao, O.; Nakai, H.; Vreven, T.; Throssell, K.; Montgomery, J.A., Jr.; Peralta, J.E.; Ogliaro, F.; Bearpark, M.J.; Heyd, J.J.; Brothers, E.N.; Kudin, K.N.; Staroverov, V.N.; Keith, T.A.; Kobayashi, R.; Normand, J.; Raghavachari, K.; Rendell, A.P.; Burant, J.C.; Iyengar, S.S.; Tomasi, J.; Cossi, M.; Millam, J.M.; Klene, M.; Adamo, C.; Cammi, R.; Ochterski, J.W.; Martin, R.L.; Morokuma, K.; Farkas, O.; Foresman, J.B.; Fox, D.J. *Gaussian 16, Revision C.01*; Gaussian, Inc.: Wallingford CT, 2016.

(63) Becke, A. D. Density-functional Thermochemistry. III. The Role of Exact Exchange. *J. Chem. Phys.* **1993**, *98* (7), 5648–5652. https://doi.org/10.1063/1.464913.

(64) Stephens, P. J.; Devlin, F. J.; Chabalowski, C. F.; Frisch, M. J. Ab Initio Calculation of Vibrational Absorption and Circular Dichroism Spectra Using Density Functional Force Fields. *J. Phys. Chem.* **1994**, *98* (45), 11623–11627. https://doi.org/10.1021/j100096a001.

(65) Frisch, M. J.; Pople, J. A.; Binkley, J. S. Self-consistent Molecular Orbital Methods 25. Supplementary Functions for Gaussian Basis Sets. *J. Chem. Phys.* **1984**, *80* (7), 3265–3269. https://doi.org/10.1063/1.447079.

(66) Bauschlicher, C. W.; Ricca, A.; Boersma, C.; Allamandola, L. J. The NASA Ames PAH IR Spectroscopic Database: Computational Version 3.00 with Updated Content and the Introduction of Multiple Scaling Factors. *ApJS* **2018**, *234* (2), 32, 1-10. https://doi.org/10.3847/1538-4365/aaa019.

(67) Boersma, C.; Bauschlicher, C. W.; Ricca, A.; Mattioda, A. L.; Cami, J.; Peeters, E.; Armas, F. S. de; Saborido, G. P.; Hudgins, D. M.; Allamandola, L. J. THE NASA AMES PAH IR SPECTROSCOPIC DATABASE VERSION 2.00: UPDATED CONTENT, WEB SITE, AND ON(OFF)LINE TOOLS. *ApJS* **2014**, *211* (1), 8, 1-12. https://doi.org/10.1088/0067-0049/211/1/8.

(68) Bauschlicher, C. W., Jr.; Boersma, C.; Ricca, A.; Mattioda, A. L.; Cami, J.; Peeters, E.; Sánchez de Armas, F.; Puerta Saborido, G.; Hudgins, D. M.; Allamandola, L. J. The NASA Ames Polycyclic Aromatic Hydrocarbon Infrared Spectroscopic Database: The Computed Spectra. *The Astrophysical Journal Supplement Series* **2010**, *189*, 341–351. https://doi.org/10.1088/0067-0049/189/2/341.

(69) Fuller, M. P.; Griffiths, P. R. Diffuse Reflectance Measurements by Infrared Fourier Transform Spectrometry. *Anal. Chem.* **1978**, *50* (13), 1906–1910. https://doi.org/10.1021/ac50035a045.

(70) Sandford, S. A.; Bernstein, M. P.; Allamandola, L. J. The Mid-Infrared Laboratory Spectra of Naphthalene (C10H8) in Solid H2O. *ApJ* **2004**, *607* (1), 346-360. https://doi.org/10.1086/383461.

(71) Szczepanski, J.; Vala, M. Infrared Frequencies and Intensities for Astrophysically Important Polycyclic Aromatic Hydrocarbon Cations. *The Astrophysical Journal* **1993**, *414*, 646–655. https://doi.org/10.1086/173110.

(72) Ribeiro da Silva, M. A. V.; Ribeiro da Silva, M. D. M. C.; Teixeira, J. A. S.; Bruce, J. M.; Guyan, P. M.; Pilcher, G. Enthalpies of Combustion of 1,4-Naphthoquinone, 9,10-Anthraquinone, 9,10-Phenanthraquinone, 1,4,9,10-Anthradiquinone, 5,8-Dihydroxy-1,4-Naphthoquinone, and 1,4-Dihydroxy-9,10-Anthraquinone. *The Journal of Chemical Thermodynamics* **1989**, *21* (3), 265–274. https://doi.org/10.1016/0021-9614(89)90016-5.

(73) Ashbourn, S. F. M.; Elsila, J. E.; Dworkin, J. P.; Bernstein, M. P.; Sandford, S. A.; Allamandola, L. J. Ultraviolet Photolysis of Anthracene in H2O Interstellar Ice Analogs: Potential Connection to Meteoritic Organics. *Meteoritics & Planetary Science* **2007**, *42* (12), 2035–2041. https://doi.org/10.1111/j.1945-5100.2007.tb01005.x.

(74) Korre, S. C.; Klein, M. T.; Quann, R. J. Polynuclear Aromatic Hydrocarbons Hydrogenation. 1. Experimental Reaction Pathways and Kinetics. *Ind. Eng. Chem. Res.* **1995**, *34* (1), 101–117. https://doi.org/10.1021/ie00040a008.

(75) Herzberg, G. *Infrared and Raman Spectra of Polyatomic Molecules*; University of Saskatchewan. D. Van Nostrand Company, Inc.: New York, 1945.

(76) Yuan, T.; Marshall, W. D. Catalytic Hydrogenation of Polycyclic Aromatic Hydrocarbons over Palladium/γ-Al2O3 under Mild Conditions. *Journal of Hazardous Materials* **2005**, *126* (1), 149–157. https://doi.org/10.1016/j.jhazmat.2005.06.022.

(77) Yuan, T.; Marshall, W. D. Catalytic Hydrogenation of Polyaromatic Hydrocarbon (PAH) Compounds in Supercritical Carbon Dioxide over Supported Palladium. *J. Environ. Monit.* **2007**, *9* (12), 1344–1351. https://doi.org/10.1039/B715318J.

(78) Yuan, T.; Fournier, A. R.; Proudlock, R.; Marshall, W. D. Continuous Catalytic Hydrogenation of Polyaromatic Hydrocarbon Compounds in Hydrogen−Supercritical Carbon Dioxide. *Environ. Sci. Technol.* **2007**, *41* (6), 1983–1988. https://doi.org/10.1021/es062194+.

(79) Nelkenbaum, E.; Dror, I.; Berkowitz, B. Reductive Hydrogenation of Polycyclic Aromatic Hydrocarbons Catalyzed by Metalloporphyrins. *Chemosphere* **2007**, *68* (2), 210–217. https://doi.org/10.1016/j.chemosphere.2007.01.034.

(80) Jacinto, M. J.; Santos, O. H. C. F.; Landers, R.; Kiyohara, P. K.; Rossi, L. M. On the Catalytic Hydrogenation of Polycyclic Aromatic Hydrocarbons into Less Toxic Compounds by a Facile Recoverable Catalyst. *Applied Catalysis B: Environmental* **2009**, *90* (3), 688–692. https://doi.org/10.1016/j.apcatb.2009.04.031.

(81) Segawa, Y.; Stephan, D. W. Metal-Free Hydrogenation Catalysis of Polycyclic Aromatic Hydrocarbons. *Chem. Commun.* **2012**, *48* (98), 11963–11965. https://doi.org/10.1039/C2CC37190A.

(82) Bresó-Femenia, E.; Chaudret, B.; Castillón, S. Selective Catalytic Hydrogenation of Polycyclic Aromatic Hydrocarbons Promoted by Ruthenium Nanoparticles. *Catal. Sci. Technol.* **2015**, *5* (5), 2741–2751. https://doi.org/10.1039/C4CY01758G.

(83) Horiuti, I.; Polanyi, M. Exchange Reactions of Hydrogen on Metallic Catalysts. *Trans. Faraday Soc.* **1934**, *30* (0), 1164–1172. https://doi.org/10.1039/TF9343001164.

(84) Onda, K.; Li, B.; Zhao, J.; Jordan, K. D.; Yang, J.; Petek, H. Wet Electrons at the H2O/TiO2(110) Surface. *Science* **2005**, *308* (5725), 1154–1158. https://doi.org/10.1126/science.1109366.

(85) Diebold, U. Perspective: A Controversial Benchmark System for Water-Oxide Interfaces: H2O/TiO2(110). *J. Chem. Phys.* **2017**, *147* (4), 040901. https://doi.org/10.1063/1.4996116.

(86) Wang, Z.-T.; Wang, Y.-G.; Mu, R.; Yoon, Y.; Dahal, A.; Schenter, G. K.; Glezakou, V.-A.; Rousseau, R.; Lyubinetsky, I.; Dohnálek, Z. Probing Equilibrium of Molecular and Deprotonated Water on TiO2(110). *PNAS* **2017**, *114* (8), 1801–1805. https://doi.org/10.1073/pnas.1613756114.

(87) Dette, C.; Pérez-Osorio, M. A.; Mangel, S.; Giustino, F.; Jung, S. J.; Kern, K. Single-Molecule Vibrational Spectroscopy of H2O on Anatase TiO2(101). *J. Phys. Chem. C* **2017**, *121* (2), 1182–1187. https://doi.org/10.1021/acs.jpcc.6b10379.

(88) Naldoni, A.; Altomare, M.; Zoppellaro, G.; Liu, N.; Kment, Š.; Zbořil, R.; Schmuki, P. Photocatalysis with Reduced TiO2: From Black TiO2 to Cocatalyst-Free Hydrogen Production. *ACS Catal.* **2019**, *9* (1), 345–364. https://doi.org/10.1021/acscatal.8b04068.

(89) Morita, K.; Yasuoka, K. Density Functional Theory Study of Atomic and Electronic Properties of Defects in Reduced Anatase TiO2 Nanocrystals. *AIP Advances* **2018**, *8* (3), 035119, 1-14. https://doi.org/10.1063/1.5021024.

(90) Cheng, H.; Selloni, A. Surface and Subsurface Oxygen Vacancies in Anatase ${\text{TiO}}_{2}$ and Differences with Rutile. *Phys. Rev. B* **2009**, *79* (9), 092101, 1-4. https://doi.org/10.1103/PhysRevB.79.092101.

(91) Zaera, F. The Surface Chemistry of Metal-Based Hydrogenation Catalysis. *ACS Catal.* **2017**, *7* (8), 4947–4967. https://doi.org/10.1021/acscatal.7b01368.

(92) Sánchez-Sánchez, C.; Martínez, J. I.; Ruiz del Arbol, N.; Ruffieux, P.; Fasel, R.; López, M. F.; de Andres, P. L.; Martín-Gago, J. Á. On-Surface Hydrogen-Induced Covalent Coupling of Polycyclic Aromatic Hydrocarbons via a Superhydrogenated Intermediate. *J Am Chem Soc* **2019**, *141* (8), 3550–3557. https://doi.org/10.1021/jacs.8b12239.

(93) Galabov, B.; Nalbantova, D.; Schleyer, P. von R.; Schaefer, H. F. Electrophilic Aromatic Substitution: New Insights into an Old Class of Reactions. *Acc. Chem. Res.* **2016**, *49* (6), 1191–1199. https://doi.org/10.1021/acs.accounts.6b00120.

(94) Hudgins, D. M.; Sandford, S. A.; Allamandola, L. J.; Tielens, A. G. G. M. Mid- and Far-Infrared Spectroscopy of Ices: Optical Constants and Integrated Absorbances. **1993**, *41*, 271, 713-870.

For TOC Only

TOC figure.